INVESTIGATING THE IMPACT OF BULK AND SURFACE RECOMBINATION ON OPEN-CIRCUIT VOLTAGE IN THIN FILM Cd(Se,Te) PHOTOVOLTAIC DEVICES: A COMPUTATIONAL APPROACH

Sakshi Gupta

A Thesis

Submitted to the Graduate College of Bowling Green
State University in partial fulfillment of
the requirements for the degree of

MASTER OF SCIENCE

July 2024

Committee:

Marco Nardone, Committee Chair

Alexy Zayak

Mikhail A Zamkov

Copyright © July 2024

Sakshi Gupta

All rights reserved

ABSTRACT

Marco Nardone, Committee Chair

Cd(Se,Te) has emerged as a leading choice for commercial thin-film PV devices, owing to their lower cost of production, high energy yields, and low degradation rates compared to silicon technology. Despite significant advancements, Cd(Se,Te) cells suffer from recombination losses, reducing the open-circuit voltage (Voc). This thesis aims to identify, distinguish, and quantify recombination losses and their locations within Cd(Se,Te) solar cells via temperature and light intensity-dependent current-voltage (JVTi) analysis. Cd(Se,Te) solar cells were modeled using COMSOL Multiphysics, simulating parameters such as temperature (T), light intensity (i), front surface recombination velocity (Sf), back surface recombination velocity (Sb), bulk lifetime (τ), conduction and valence band offset (CBO and VBO at heterojunctions), and back contact Schottky barrier height (Φbp). Additionally, graded and uniform selenium devices were studied, and ZnTe:Cu was investigated as a back contact interface.

In this work, recombination activation energies, Ea, from JVTi studies were shown to quantify the front interface conduction band offset losses when the interface band gap is smaller than the bulk band gap and when front interface recombination dominates. If the Ea equals the bulk band gap, then Voc losses may occur at the front interface or within the bulk. When the front surface recombination and bulk lifetime are moderately low, a transition from front surface (low Ea) to bulk (higher Ea) mechanisms can be observed with increasing light intensity, i. Back surface recombination has negligible effects on Voc for the device parameters specified herein. Comparison of Cd(Se,Te) JVTi data provided by NREL to simulations in this work indicates that front surface recombination dominates Voc losses for Sf = 103 cm/s and CBO = -0.2 eV for that particular device. Adjusting the band alignment to CBO = 0 eV and reducing Sf would significantly increase Voc.

I would like to dedicate this work to my parents and grandparents. They are my inspiration, motivation, and support system. Love you. <3

ACKNOWLEDGMENTS

I would like to thank my research advisor, Dr. Marco Nardone for his guidance, support, and the knowledge imparted throughout my Master's program. I will be forever grateful. Thank you to Dr. Zayak and Dr. Zamkov for being part of my committee, and for teaching and advising me. My parents and family have been my biggest source of motivation, encouraging me to work hard every step of the way and be the best version of myself.

I would like to thank my roommate and best friend, Eva Mulloy, who is also writing a physics thesis, for all the lovely baked goods and physics peer support. Thank you to my boyfriend Varun, who was always there for me and tolerated my daily shenanigans, and listened to me ramble on about my thesis. Thank you to the printer in the lab. Grateful for frozen food that kept me going. Thank you caffeine.

This thesis was developed based on funding from the Department of Energy Office of Energy Efficiency and Renewable Energy Solar Energy Technologies Office and the National Renewable Energy Laboratory.

A big thanks to the entire Physics and Astronomy Department at Bowling Green State University. Thank you to all the people who have made this possible!

TABLE OF CONTENTS

Page

CHAPTER 1 INTRODUCTION 1

1.1 History of Photoelectric Devices 1

1.2 Thin-Film PV Devices 1

1.3 Research Objective 5

CHAPTER 2 BACKGROUND PHYSICS 7

2.1 Open-Circuit Voltage 7

2.2 Charge Transport Theory 8

2.3 Recombination 10

2.3.1 Radiative Recombination 10

2.3.2 Trap-assisted or SRH Recombination 12

2.3.3 Auger Recombination 13

2.3.4 Surface Recombination 14

2.4 Lifetime Equations 15

2.5 Temperature Dependent Parameters 16

2.6 Band Offset at Heterojunctions 17

2.7 Activation Energy 18

CHAPTER 3 METHODOLOGY 20

3.1 NREL Cd(Se,Te) Devices 20

3.2 Device Simulation 25

3.2.1 Parameter Space 29

3.2.2 JVTi Methodology 33

CHAPTER 4 RESULTS AND DISCUSSION 35

4.1 Se-graded Device With Buffer Layer: JVTi Study 36

4.2 Se-graded Device Without Buffer Layer: JVTi Study 42

4.2.1 Back Contact Study 45

4.2.2 Incorporation of ZnTe:Cu as Back Contact Interface 46
4.3 Uniterns: Uniform Se Device Without Buffer Layer 48
4.4 Comparing Simulations with Experimental Data 50
CHAPTER 5 CONCLUSIONS 52
CHAPTER 6 FUTURE WORK 54
BIBLIOGRAPHY 55
APPENDIX A 3D Plots: E_a vs. S_f vs. τ 60
APPENDIX B JVTi: V_{oc} vs. T plots 64

LIST OF FIGURES

Figure Page

1.1 PV device efficiency evolution chart 2

1.2 CdTe solar cell device stack and CBO and VBO alignment 3

2.1 Recombination mechanisms prevalent in solar cells leading to energy losses 11

2.2 Surface recombination due to the presence of surface traps 14

2.3 Conduction Band Offset (CBO) and Valence Band Offset (VBO) energy diagram . 18

3.1 As deposited material stack and processing leading to the completed superstrate configuration As-doped Cd(Se,Te) device stack. 20

3.2 Secondary ion mass spectroscopy (SIMS) profiles data of Se profiles for V401 and V617. (Courtesy: NREL) 22

3.3 Carrier concentration vs. depletion width for NREL Devices V401 and V617 obtained from capacitance vs. voltage measurements 23

3.4 External Quantum Efficiency for NREL Devices V401 and V617 24

3.5 JV Curve for NREL Devices V401 and V617 24

3.6 Cd(Se,Te) Device: (1) SnO_2:F TCO Layer (2) SnO_2 Buffer Layer (3) Cd(Se,Te) Absorber Layer (4) ZnTe:Cu Back Contact Interface 26

3.7 Selenium grading as a function of depth into the device x. The y-axis is the selenium alloy fraction, with a maximum of 30% Se in the Cd(Se,Te) absorber layer. . 26

3.8 Bandgap function $E_g(y)$ in eV for Cd(Se,Te), with the x-axis as the Se fraction in the Cd(Se,Te) absorber layer 27

3.9 Electron affinity function $\chi(y)$ for Cd(Se,Te), with the x-axis as the Se fraction in the Cd(Se,Te) absorber layer 28

3.10 Bandgap energy as a function of the device depth, x coordinate 29

3.11 Energy band diagram showing the electron affinity χ and Schottky barrier Φ_{bp}. . . . 31

4.1 Breakdown of the studies reported herein. Roman numerals correspond to the parameter spaces investigated as listed in Section 3.2.1. 35

4.2 Simulated room temperature (T = 300 K) JV curves for Cd(Se,Te) device over a range of front surface recombination velocities. 36

4.3 V_{oc} vs. T to extract the activation energy E_a from the y-intercept for a range of front surface recombination velocities and CBO = 0 eV, i = 1 Sun, and τ = 1 ns. . . 37

4.4 E_a vs. τ vs. S_f for CBO = 0 eV and i = 1 Sun 38

4.5 E_a vs. τ vs. S_f at i = 1 Sun, for CBO = ΔE_c = -0.4, -0.2, 0, 0.2 eV. 39

4.6 V_{oc} vs. CBO at T = 325 K, S_f = 1000 cm/s, τ = 100 ns, and at various light intensities shown in the legend. V_{oc} declines as CBO becomes increasingly negative. 40

4.7 E_a vs. τ vs. S_f for i = 1, 0.1, 0.01 Sun at CBO = ΔE_c = -0.2 eV. 41

4.8 (a) E_a vs. light intensity i at CBO = -0.2 eV and S_f = 1000 cm/s for τ = 1 to 10^3 ns. (b) V_{oc} vs. light intensity i at T = 325 K, S_f = 1000 cm/s, τ = 100 ns for CBO = -0.4, -0.2, 0, 0.2 eV 42

4.9 V_{oc} vs. T: with SnO_2 and the without SnO_2 buffer layer. 43

4.10 Room temperature JV curve without buffer layer at S_f = 100 cm/s, τ = 5 ns, CBO = -0.2 eV, and Φ_{bp} = 0.4 eV 44

4.11 Back contact study: V_{oc} vs. T for $\Phi_{bp} = 0.2$ and 0.4 eV. Parameters: CBO = 0 eV, i = 1 Sun, τ = 1000 ns, S_f = 100 cm/s. 45

4.12 V_{oc} vs. T for VBO = 0 eV and -0.4 eV with added ZnTe:Cu interface. 46

4.13 E_a with changing VBO at various back surface recombination velocities, S_b, and back contact barriers. 47

4.14 V_{oc} vs. T plots for Uniterns - 0% Se 48

4.15 V_{oc} vs. T plots for Uniterns - 20% Se and 40% Se. 49

4.16 $V_{oc}(T)$ for a range for light intensities i = 0.02 - 1.78 Suns. 50

4.17 V_{oc} (T) at i = 1 Sun and CBO = ΔE_c = -0.2 eV. 51

1 E_a vs. S_f vs. τ plots: CBO = -0.4 eV, i = 1, 0.1, 0.01 Suns 60

2 E_a vs. S_f vs. τ plots: CBO = -0.2 eV, i = 1, 0.1, 0.01 Suns 61

3 E_a vs. S_f vs. τ plots: CBO = 0 eV, i = 1, 0.1, 0.01 Suns 62

4 E_a vs. S_f vs. τ plots: CBO = 0.2 eV, i = 1, 0.1, 0.01 Suns 63

5 V_{oc} vs. T for CBO = 0 eV, i = 1 Sun 65

6 V_{oc} vs. T for CBO = 0 eV, i = 0.1 Sun 66

7 V_{oc} vs. T for CBO = 0 eV, i = 0.01 Sun 67

8 V_{oc} vs. T for CBO = 0.2 eV, i = 1 Sun 68

9 V_{oc} vs. T for CBO = 0.2 eV, i = 0.1 Sun 69

10 V_{oc} vs. T for CBO = 0.2 eV, i = 0.01 Sun 70

11 V_{oc} vs. T for CBO = -0.2 eV, i = 1 Sun 71

12 V_{oc} vs. T for CBO = -0.2 eV, i = 0.1 Sun 72

13 V_{oc} vs. T for CBO = -0.2 eV, i = 0.01 Sun 73

14 V_{oc} vs. T for CBO = -0.4 eV, i = 1 Sun 74

15 V_{oc} vs. T for CBO = -0.4 eV, i = 0.1 Sun 75

16 V_{oc} vs. T for CBO = -0.4 eV, i = 0.01 Sun 76

LIST OF TABLES

Table Page

3.1 Structural differences in V401 and V617 21

3.2 Cd(Se,Te) device parameters for COMSOL set-up. 25

3.3 Parameter space for Se-graded device model with buffer layer 30

3.4 Parameter space for Se-graded device model without buffer layer 30

3.5 Parameter space for back contact study: Se-graded device model without buffer layer 31

3.6 Parameter space for new back contact interface: Se-graded device without buffer layer 32

3.7 Parameter space for Uniterns: Uniform Se device without buffer layer 33

4.1 Activation energies for CBO = 0 eV, i = 1 Sun and τ = 1 ns over a range of temperatures and S_f. Note: Row T = 300 K corresponds to the V_{oc} values in Fig. 4.2. . . 38

4.2 Comparison of E_a values with and without the SnO_2 buffer layer. Note: The ΔE_a column is in units of meV. The linear regression fitting error in E_a is about 10 meV. 43

4.3 Comparison of V_{oc} values for Se-graded device model with and without the SnO_2 buffer layer for a range of back surface recombination (S_b) values. V_{oc} does not depend on S_b. 44

CHAPTER 1 INTRODUCTION

1.1 History of Photoelectric Devices

With the rapid increase in global power consumption, shifting towards renewable energy, such as solar energy, to offset the repercussions of incessantly burning fossil fuels is imperative. The discovery of the photovoltaic effect (1839), the photoconductivity of selenium (1873), and the photoelectric effect (1905), along with other major scientific milestones, paved the way for the birth of photovoltaic (PV) technology in the United States at Bell Labs (1954) [1]. In 2022, the world consumed almost 179 thousand TWh of power, with a contribution of approximately 2% from solar energy [2]. Provided that energy systems are completely decarbonized, the National Renewable Energy Labs (NREL) expects 45% of the electricity consumption in the US to be solar-powered by 2050, accompanied by declining costs [3]. The United States installed 11.8 GW (direct current) of PVs in the first half (H1) of 2023—the largest H1 ever [4].

There are broadly three categories of solar cells – monocrystalline, polycrystalline, and thin-film solar cells. There are two types of thin-film solar cells dominating the market, namely cadmium telluride (CdTe) and copper indium gallium diselenide (CIGS). After crystalline silicon-based cells, CdTe thin films are the most popular with a market share of about 10%, and have the lowest manufacturing cost. The theoretical limit of efficiency in solar cells, also known as the detailed balance limit, represents the maximum theoretical efficiency that a solar cell could achieve under ideal conditions, assuming perfect energy balance and no non-radiative losses [5]. Fig. 1.1 shows that CdTe research cells have reached efficiencies of 22.6%, while the theoretical limit is approximately 30% [6].

1.2 Thin-Film PV Devices

Cadmium Telluride cells have emerged as the leading technology for commercial thin-film PV devices, owing to their better cost of production, energy yields, low degradation rates, and temperature coefficients compared to silicon technology [8]. The addition of an 800 nm Cd(Se,Te) layer to the CdTe absorber lowered a portion of the device bandgap to 1.41eV, enabling the

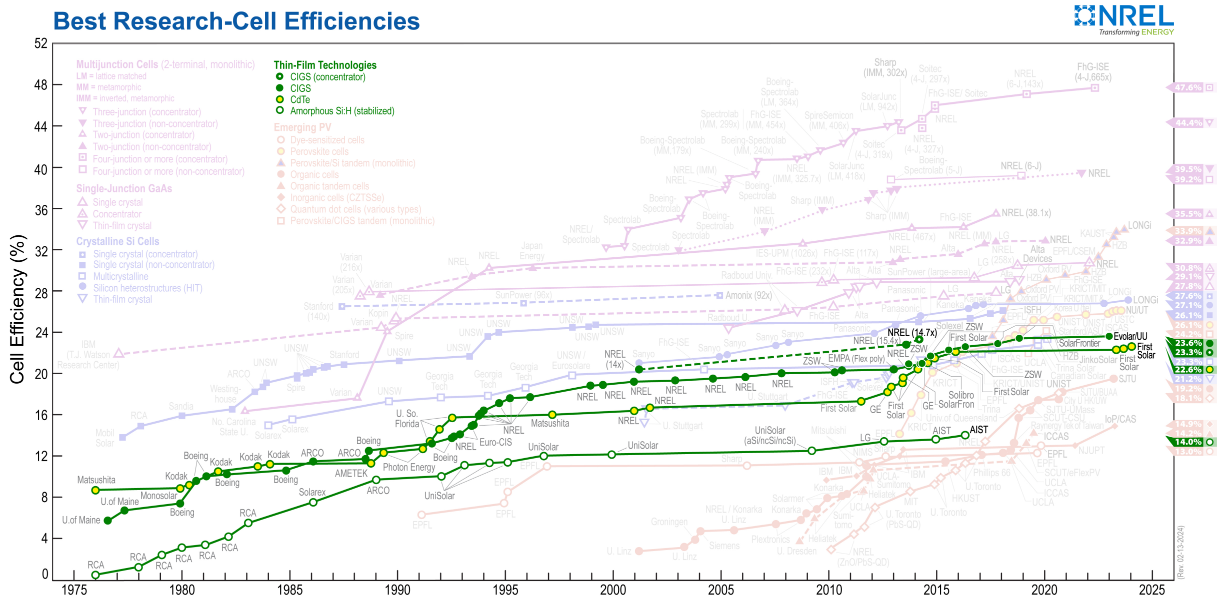

Figure 1.1 Best research PV device efficiency evolution chart showing CdTe devices achieving efficiencies of $\approx$ 22.6% with $\approx$ 6% increase in CdTe efficiencies in the last 15 years [7].

current density to increase from 26 to over 28 mA/cm^2 [9]. For a bandgap of 1.4 eV, eliminating the CdS window layer and replacing it with alternate emitter layers such as Metal Conducting Oxides ($Mg_xZn_{x-1}O$) and Cd(Se,Te) absorber layers contributed to increasing efficiencies [10]. However, low V_{oc} remains a bottleneck in increasing device efficiencies. Studying the open-circuit voltage (V_{oc}) specifically has key advantages: firstly, calculating recombination currents becomes more straightforward because they balance with the forward photocurrent (Kirchhoff's Current Law), and secondly, the impact of series resistance is minimized since no net current flows in the open-circuit condition. When modeling V_{oc} as a function of temperature and illumination, understanding the mathematical forms of the various recombination mechanisms is important [11]. These equations are described in Sections 2.3, 2.4, and 2.5. Within the detailed balance limit, a band gap E_g $\approx$1.4 eV for alloyed Cd(Se,Te) should give a V_{oc} of 1.140, yet the V_{oc} remains at or below 850–900 mV for all but a few state of the art devices [12].

Group V dopants have been found to be more stable and can achieve V_{oc} greater than 1 V only in single crystalline devices, which is the collective goal for Cd(Se,Te) thin-film devices [13]. Additionally, it was demonstrated that devices with As doping degrade significantly slower

as compared to Cu doping in accelerated lifetime testing [14]. Metzger et al. in 2022 [15] reported that the efficiency of As-doped solar cells is on par with Cu-doped cells, with efficiencies of 22% based on NREL's certification results, and between 22.2% and 22.4% by their internal testing. Moreover, the normalized efficiency temperature coefficient [$(\Delta\eta/\eta)$/ΔT] was reduced to -0.23%/°C whereas the typical values for Si-based cells is between -0.30%/°C and -0.45%/°C. Colegrove et al. [16] showed that co-doping As and Cu can boost the V_{oc} and device performance. They found that Cu may be able to reduce bulk recombination while having no impact on the carrier concentration in the bulk. Arsenic doping is a promising direction in thin-film technologies.

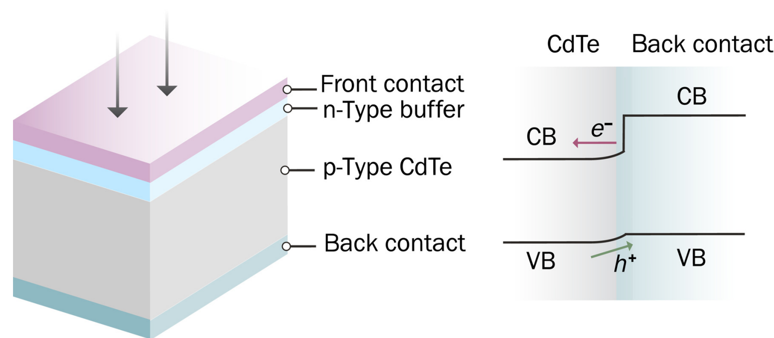

Figure 1.2 CdTe solar cell and band alignment showing the conduction and valence band offset at the CdTe/back contact interface. Left: Device stack in superstrate configuration with solar irradiation falling on the front contact. Right: Desired band alignment between p-type CdTe absorber layer and the back contact facilitating barrierless hole transport and electron reflection [17].

In the context of back contacts of the device, a suitable material for a superstrate CdTe solar cell must meet specific design criteria [17]:

(i) chemically stable interaction with CdTe,

(ii) high hole mobility (μ_p) and a favorable hole-to-electron mobility ratio for efficient hole transport away from the interface,

(iii) ideal valence band (VB) alignment (See Fig. 1.2) with CdTe, typically within 0 to 0.3 eV to minimize barriers for hole transport and enhance fill factor,

(iv) appropriate conduction band (CB) alignment (See Fig. 1.2), higher CB minimum than that of CdTe to enable electron reflection at the interface,

(v) capability for p-type doping to introduce hole carriers and align the Fermi energy at the interface, and

(vi) absence of detrimental deep interface states that lead to non-radiative carrier recombination.

Cu-doped ZnTe (ZnTe:Cu) is popularly used as the hole-selective p-doped back contact in commercial thin-film CdTe solar cells. Calculations propose that ZnTe's band alignment is almost ideal, with a VBO = 0.03 eV and a much higher conduction band due to its bandgap of 2.2 eV. It was concluded that band bending at the back interface is beneficial for barrierless hole transport from CdTe into ZnTe, as well as for electron reflection. However, there is a large enough lattice mismatch between the ZnTe and CdTe planes to cause multiple consequences, such as strained ZnTe near the interface, formation of deep-level defect states, and other interface defects [18].

While major strides have been made, thin-film Cd(Se,Te) devices are still riddled with recombination losses, resulting in lower V_{oc} values. Minimizing recombination losses necessitates diverse approaches in device engineering, material enhancement, and computational analysis. For instance, refining the buffer layer to mitigate surface recombination, exploring alternative back contact structures, and employing various doping strategies, among others. It is essential to identify and quantify recombination losses, pinpointing the primary locations of each recombination type. This identification enables the application of targeted tactics to specific regions of the solar cell, thus enhancing overall performance.

One method for analyzing recombination in photovoltaic (PV) devices involves temperature-dependent current-voltage measurements (JVT). It can potentially recognize the prevailing recombination mechanism through the activation energy E_a extracted from the intercept of V_{oc} at $T = 0$ K. A more comprehensive approach involves incorporating the light intensity (i) dependence on V_{oc} (JVTi) [19]. The dominant recombination paths of CdTe solar cells with different buffer layers were investigated through temperature-dependent current-voltage (JVT) characterization in both light and dark conditions, using traditional CdS/CdTe devices as a reference [20]. Fang et al. explain that the E_a extracted from light JVT measurements introduces fewer errors since it does not require the parameters of the one-diode model. These parameters

are described in Section 2.1. In contrast, extracting E_a from dark JVT measurements requires calculating the parameters such as the ideality factor A, and the saturation current J_0, which can negatively affect the E_a value. However, this has minimal impact on the results, making both methods reliable. Furthermore, the back-contact barrier height can be determined from JVT experiments and was validated using conventional admittance spectroscopy [21]. Mia et al. (2018) used dark JVT measurements to estimate the back-contact barrier height, a critical factor in CdTe devices. The defect energies obtained from admittance spectroscopy (CdSe: 321.5 ± 8.6 meV) and JVT measurements (CdSe: 329.4 ± 8.3 meV) are in close agreement.

1.3 Research Objective

In this thesis, Cd(Se,Te) solar cells were modeled using COMSOL Multiphysics, simulating a range of parameters such as temperature (T), light intensity (i), front surface recombination velocity (S_f), back surface recombination velocity (S_b), bulk lifetime (τ), and Schottky barrier height (Φ_{bp}). Various back contact structures, valence and conduction back offsets (VBO and CBO), and doping strategies with selenium and arsenic were also studied. In order to visualize the transition between the bulk and surface recombination-dominated regions, activation energies (E_a) were extracted from JVTi studies within a broad parameter space and plotted for a range of carrier lifetimes (τ) and front surface interface recombination velocities (S_f). Simulation results were then compared with data from Cd(Se,Te) devices fabricated at NREL. The objective of this research is to better understand how JVTi measurements and modeling can distinguish and quantity recombination losses in thin-film PV devices.

Chapter 2 details the pertinent background physics, workings of a solar cell, efficiency and the open circuit voltage (V_{oc}), charge transport theory and various recombination mechanisms, carrier lifetimes, activation energy (E_a), and band offset at heterojunctions. Chapter 3 describes the Cd(Se,Te) device structure in our simulations, NREL devices (V401 and V617), and the COMSOL set-up including the parameter space for each set of simulations. The results are discussed in Chapter 4 and are divided into two main studies: (1) Se-graded devices with and without a SnO_2 buffer layer and (2) uniform Se devices (Uniterns). The simulation results are

compared with the empirical data provided. Chapter 5 draws conclusions followed by future work in Chapter 6.

CHAPTER 2 BACKGROUND PHYSICS

2.1 Open-Circuit Voltage

Solar cells work on the principles of the photovoltaic effect, converting light energy into electricity. When an electron gains energy equal to its band gap (E_g) from a light source, the electrons break free of their bound state and can now participate in conduction. This is known as generation. The maximum current output of a solar cell is determined by the optical properties of the materials used. The absorption coefficient (α) indicates how far into the material light of a certain wavelength can travel before it is absorbed. The short circuit current (I_{sc}) flows through the circuit when the voltage across the circuit is zero. I_{sc} depends on the incident light spectrum and the area of the cell. The short circuit current density ($J_{sc} = I_{sc}$/Area) is often used since it eliminates the dependence on the surface area and is an important parameter to describe the efficiency of a device [22]. Another vital parameter to focus on is the open-circuit voltage (V_{oc}), which is the voltage across the circuit when no current is flowing i.e. when the circuit is open and it is given by:

$$V_{oc} = \frac{kT}{q} \ln\left(\frac{J_{sc}}{J_0} + 1\right) \qquad \text{where} \qquad J_0 = J_{00} \exp\left(\frac{-E_a}{AkT}\right) \tag{2.1.1}$$

Here, kT is the product of the Boltzmann constant and temperature while q is a unit charge. The saturation current J_0 is the current in the circuit that flows in reverse bias caused by carriers generated thermally and J_{00} is the exponential factor for J_0. It is closely related to the diode ideality factor A, which describes the deviation of a device from the ideal case ($A = 1$) [23]. The activation energy E_a refers to the energy barrier carriers need to overcome to move freely in the material. Substituting J_0 into the first equation gives us:

$$V_{oc} = \frac{E_a}{q} - A\frac{kT}{q} \ln\left(\frac{J_{00}}{J_{sc}}\right) \tag{2.1.2}$$

Note that upon plotting V_{oc} vs. T, the activation energy can be calculated from the y-intercept. The efficiency of a solar cell is the ratio of the maximum power output and the power input and is given by the equation:

$$\eta = \frac{V_{oc} J_{sc} FF}{P_{in}} \qquad \text{where} \qquad FF = \frac{V_{MP} J_{MP}}{V_{oc} J_{sc}} \tag{2.1.3}$$

The Fill Factor (FF) determines the maximum power of a solar cell, and MP stands for Maximum Power.

2.2 Charge Transport Theory

In this section, the generation of electron-hole pairs, drift, and diffusion current, the continuity equations, and Poisson's equations will be described [24] [25] [26]. Generation of Electron Hole Pairs (EHP) requires a minimum amount of energy, which is usually equal to the band-gap energy E_g. The processes that generate EHPs are ionization on impact, thermal generation, photogeneration, and impurity-mediated generation. Most of the generation in solar cells takes place via photogeneration. The total generation rate $G(x)$ at a depth x, after accounting for reflective loss from the front surface, can be found by integrating over all the energies giving us:

$$G(x) = \int_{E_g}^{\infty} [1 - R(E)]\alpha(E)\Gamma_0(E)e^{-\alpha(E)x} dE \tag{2.2.1}$$

where $R(E)$ is the reflectance as a function of energy E, α is the absorption coefficient describing the probability that a photon of energy E is absorbed, and Γ_0 is the incident flux (photons/cm$^2/s$).

The carrier motion inside an electric field creates a **drift current**. In other words, the free carriers in the device will accelerate parallel or anti-parallel to the electric field, creating the drift current. The drift current density $\mathbf{J}_{drift}$ (A/cm^2) can be expressed as:

$$\mathbf{J}_{drift} = \mathbf{J}_{n,drift} + \mathbf{J}_{p,drift} = (nq\mu_n + pq\mu_p)\mathbf{E} = \sigma_s \mathbf{E} \tag{2.2.2}$$

where n and p are the number densities of electrons and holes respectively, μ is the carrier

mobility (cm^2/V s), q is the elementary charge, and **E** is the electric field. The proportionality constant relating $\mathbf{J}_{drift}$ and **E** is called the conductivity σ_s (Siemens/cm), and its inverse is called resistivity ρ_s (Ω-cm). Additionally, a concentration gradient of free carriers inside a semiconductor creates a **diffusion current**, $\mathbf{J}_{diff}$. In three dimensions, the diffusion current for electrons and holes using the gradient can be written as:

$$\mathbf{J}_{diff} = \mathbf{J}_{n,diff} + \mathbf{J}_{p,diff} = qD_n\nabla n - qD_p\nabla p \tag{2.2.3}$$

where D_n and D_p are the electron and hole diffusion coefficients, respectively. They are the proportionality constants for the positive relationship between particle flux and concentration gradient. The total free carrier current is given by the sum of each type of particle $\mathbf{J}_{Total} = \mathbf{J}_p + \mathbf{J}_n$. The total carrier current for each type of particle can be written as the sum of the drift and diffusion currents:

$$\mathbf{J}_n = q\mu_n n\mathbf{E} + qD_n\frac{\partial n}{\partial x}\hat{x} \tag{2.2.4}$$

$$\mathbf{J}_p = q\mu_p p\mathbf{E} - qD_p\frac{\partial p}{\partial x}\hat{x} \tag{2.2.5}$$

Carrier movement can be further described by coupling the Poisson equation and continuity equations for electrons and holes. In Poisson's equation, $\nabla^2 V = -\rho/\epsilon$, substitute the charge density, $\rho = q(p - n - N_A^- + N_D^+ \pm N_t^{+/-})$ to get:

$$\nabla^2 V = -\frac{q}{\epsilon}(p - n - N_A^- + N_D^+ \pm N_t^{+/-}) \tag{2.2.6}$$

where V is the electrical potential, ϵ is the permittivity for the semiconductor, N_A is the acceptor (hole) density, N_D is the donor (electron) density, and N_t is the density of charge traps. The time-dependent electron and hole continuity equations are:

$$\frac{\partial n}{\partial t} - \frac{1}{q}\nabla \cdot \mathbf{J}_n = G_n - U_n \tag{2.2.7}$$

$$\frac{\partial p}{\partial t} - \frac{1}{q}\nabla \cdot \mathbf{J}_p = G_p - U_p \tag{2.2.8}$$

where U_n and U_p are the net rates of electron and hole recombination respectively. Together, the drift-diffusion, continuity, and Poisson's equations (Eqs. (2.2.4) to (2.2.8)), describe the physical mechanisms in solar cells and give us insight into the electrical potential, the density of electrons and holes (n and p), and the electric field.

2.3 Recombination

To bring a system back to equilibrium, recombination of electrons and holes occurs. It is the opposite of generation and involves the annihilation of an electron-hole pair. Recombination reduces the number of free charge carriers, limiting the efficiency of the device. In addition to recombination on the surface of the device, there are three types of recombination in the bulk of the device, namely: Radiative, trap-assisted (or Shockley-Read-Hall), and Auger recombination.

2.3.1 Radiative Recombination

Radiative recombination occurs when an electron from the conduction band recombines with a hole in the valence band, releasing a photon that possesses energy equal to that of the bandgap. Refer to Fig. 2.1(a). In this case, the net rate of radiative recombination can be expressed as the difference between the radiative recombination rate R_{rad}, and the thermal generation rate G_{th} as $U_{rad} = R_{rad} - G_{th}$ Writing in terms of the radiative recombination coefficient C, $R_{rad} = Cnp$, and $G_{th} = C(n_i)^2$, where n_i^2 is the intrinsic electron density (np $\neq n_i^2$). The equation is thus:

$$U_{rad} = Cnp - Cn_i^2 = C(np - n_i^2) \tag{2.3.1}$$

The first term describes the non-equilibrium electron-hole population (from illumination), while the second term holds the intrinsic thermal carrier population. For a p-type material at low-level injection $N_A = p_0 >> n_0$, with normal light $np >> n_i^2$, the excess electron-hole density is

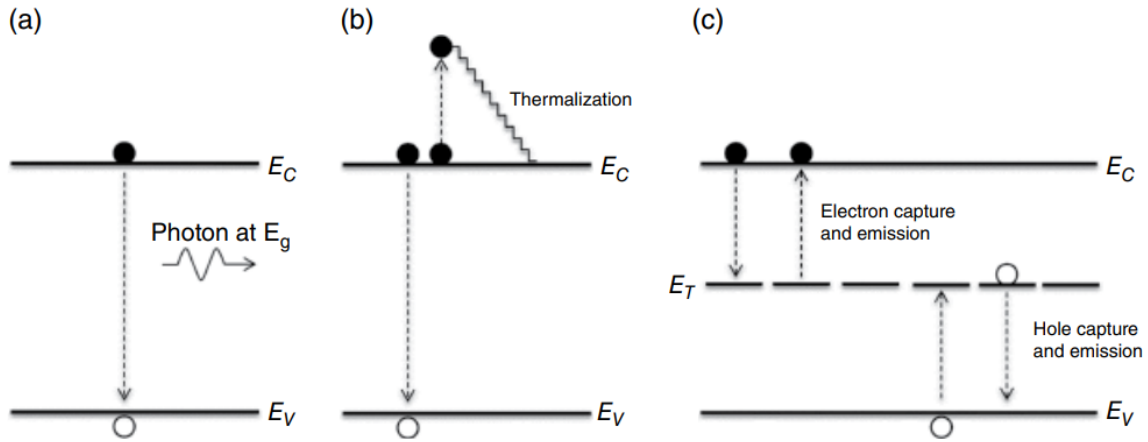

Figure 2.1 Recombination mechanisms prevalent in solar cells leading to energy losses (a) Radiative band-to-band recombination: electrons in the conduction band recombine with holes in the valence band, emitting a photon (b) Non-radiative Auger recombination: electron recombines with a hole, transfers its energy to another electron, exciting that second electron to a higher energy state (c) Non-radiative trap-assisted (SRH) recombination: electron recombines with a hole through defect states, releasing thermal energy [27].

$\Delta n = n - n_0 \approx n$, and Eq. (2.3.1) can be written as:

$$U_{rad} = C\Delta n N_A \qquad \text{for} \qquad \Delta n << N_A \tag{2.3.2}$$

where N_A is the acceptor density. At high-level injection ($\Delta n \approx \Delta p$), U_{rad} is expressed as:

$$U_{rad} = C\Delta n\Delta n = C(\Delta n)^2 \qquad \text{for} \qquad \Delta n >> N_A \tag{2.3.3}$$

The *lifetime* of a carrier is defined as the average time it spends in the excited state before it recombines. The known general lifetime equation is given by:

$$\tau \equiv \frac{\Delta n}{U_i}, \tag{2.3.4}$$

where U_i is the net recombination rate for a generic mechanism. With this lifetime equation and Eqs. (2.3.2) and (2.3.3), the radiative lifetime for both low and high injection cases can be expressed as:

$$\tau_{rad,low} = \frac{1}{CN_A} \qquad \text{for} \qquad \Delta n << N_A \tag{2.3.5}$$

$$\tau_{rad,high} = \frac{1}{C\Delta n} \qquad \text{for} \qquad \Delta n >> N_A \tag{2.3.6}$$

2.3.2 Trap-assisted or SRH Recombination

Trap-assisted (or Shockley-Read-Hall) recombination occurs at trap sites created within the bandgap of the devices due to impurities and/or vacancies. Electrons and holes use these gap defects to cross the bandgap to recombine and release energy in the form of lattice vibrations, making it a non-radiative recombination mechanism. Fig. 2.1(c) shows this phenomenon and the recombination centers in the middle of the band gap. SRH recombination and generation involves four steps: electron capture, hole capture, electron emission, and hole emission. The net rate of SRH recombination is given by:

$$U_{SRH} = \frac{np - n_i^2}{\tau_{n_0}(p + p_1) + \tau_{p_0}(n + n_1)} \tag{2.3.7}$$

where τ_{n_0} and τ_{p_0} are the minimum electron and hole SRH-lifetimes respectively. The effective electron and hole densities, n_1 and p_1 respectively, assuming that the Fermi-level lies on the defect, are given by:

$$n_1 \equiv n_i e^{\left(\frac{E_t - E_i}{kT}\right)} \qquad \text{and} \qquad p_1 \equiv n_i e^{\left(\frac{E_i - E_t}{kT}\right)} \tag{2.3.8}$$

where E_i is the intrinsic Fermi energy level, and E_t is the trap energy level. Trap energy levels can be either discrete or continuous [28]. The intrinsic electron concentration can be expressed as $n_i = \sqrt{N_C N_V}\text{exp}(-E_g/2kT)$, showing the dependence on the bandgap E_g, and the effective densities of states (DOS) in the conduction and valence bands, N_C and N_V respectively. Similar to radiative recombination, Eq. (2.3.4) and Eq. (2.3.7) can be used to express the SRH lifetimes under low and high injection conditions as follows:

$$\tau_{SRH,low} \approx \tau_{n_0} \qquad \text{for} \qquad \Delta n << N_A \tag{2.3.9}$$

$$\tau_{SRH,high} \approx \tau_{n_0} + \tau_{p_0} \qquad \text{for} \qquad \Delta n >> N_A \tag{2.3.10}$$

The capture time constants for electrons and holes, τ_{n_0} and τ_{p_0}, are defined as:

$$\tau_{n_0} \equiv \frac{1}{\sigma_n v_{th} N_t} \qquad \text{and} \qquad \tau_{p_0} \equiv \frac{1}{\sigma_p v_{th} N_t} \tag{2.3.11}$$

where σ_n and σ_p are the capture cross-section of the electrons and holes respectively, v_{th} is the thermal velocity of the carriers, and N_t is the density of the trap sites. Note that the thermal velocity is $v_{th} = \sqrt{3kT/m}$, where m is the mass of the electron. Using this definition, Eq. (2.3.10) can be rewritten for high-injection level ($\Delta n >> N_A$):

$$\tau_{SRH} \approx \tau_{n_0} + \tau_{p_0} = \frac{\sigma_n + \sigma_p}{\sigma_n \sigma_p v_{th} N_t} \tag{2.3.12}$$

2.3.3 Auger Recombination

Auger recombination involves three carriers, as opposed to the typical electron-hole pair recombination. After an electron and hole combine, the energy is given to a third carrier, an electron (or hole) in the conduction band (or valence band). Fig. 2.1(b) shows that this electron (or hole) is further excited in the conduction band (or valence band), after which it loses its energy to lattice vibrations and thermalizes down to the edge of the conduction (or valence) band. A possible classification based on the carriers involved can be: electron-electron-hole (eeh) and electron-hole-hole (ehh) recombination. This three-carrier recombination requires a high carrier density, which means it mostly occurs at high injection levels. The net rate of Auger recombination is given by:

$$U_{Aug} = (C_{n,Aug} n + C_{p,Aug} p)(np - n_i^2) \tag{2.3.13}$$

where $C_{n,Aug}$ and $C_{p,Aug}$ are the Auger recombination coefficients for electrons and holes respectively. At high injection levels, Eq. (2.3.13) can be simplified to:

$$U_{Aug} \approx C_{Aug} \Delta n^3 \quad \text{for} \quad \Delta n \approx \Delta p >> N_A \tag{2.3.14}$$

where C_{Aug} is the Auger coefficient. Then, using Eq. (2.3.4) and (2.3.14), the Auger lifetime equation is:

$$\tau_{Aug} = \frac{1}{C_{Aug} \Delta n^2} \tag{2.3.15}$$

2.3.4 Surface Recombination

Surface recombination in semiconductors poses a critical challenge to the efficiency of solar cells. At the interface of a solar cell, the presence of dangling unpassivated bonds, a disrupted lattice, and structural impurities form a dense array of trap states, as depicted in Fig. 2.2. These trap states are almost continuously distributed across the bandgap. These states serve as an unlimited source or sink for carrier recombination and generation and can cause significant energy losses if left unpassivated. Similarly, the interfaces between different semiconductor materials also contribute to recombination due to the presence of interface states, although, to a lesser extent. Surface recombination is similar to SRH recombination due to the presence of traps

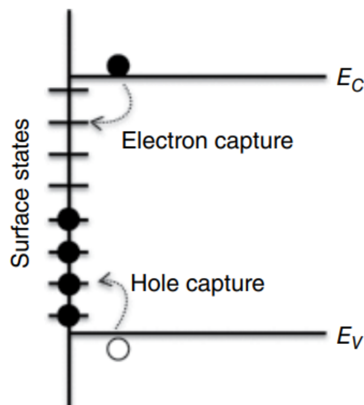

Figure 2.2 Facilitation of electron and hole capture due to the presence of surface trap states at the surface of a semiconductor, thus increasing recombination at the surface and decreasing the efficiency of the device [27].

in both cases. Analogous to SRH, the net recombination rate can be written by replacing τ_n and τ_p with $1/S_n$ and $1/S_p$, where S_n and S_p are the surface recombination velocities (cm/s) for electrons and holes respectively:

$$S_n \equiv \sigma_n v_{th} N_t \quad \text{and} \quad S_p \equiv \sigma_p v_{th} N_t \tag{2.3.16}$$

where σ_n is the capture cross section, and v_{th} is the thermal velocity, and N_t is the density of trap sites at the surface. The net surface recombination rate is given by: $U_s = \Delta n_s/\tau_s$. If the interface has excess recombination sites, then the excess carrier concentration will be lower at the surface than in the bulk. This causes a net current to flow toward the semiconductor's surface, subsequently removing carriers from the desired path. When the carrier mobility is high enough, then the carriers for surface recombination are collected at the depths of the material, making it dependent on the thickness (d). The net surface recombination is:

$$U_s = \frac{\Delta n_s}{d/S} \tag{2.3.17}$$

To gain a deeper insight into the mobility of carriers the diffusion of carriers can be incorporated, rewriting Eq. (2.3.17) as:

$$U_s = \frac{\Delta n_s}{\frac{d}{S} + \frac{d^2}{D_n}} \tag{2.3.18}$$

where $D_n = \mu_n(kT/q) = V_{th}\mu_n$. The total lifetime then for the surface can be expressed as:

$$\tau_{Surface} = \frac{d}{S} + \frac{d^2}{D_n} \tag{2.3.19}$$

2.4 Lifetime Equations

The minority-carrier lifetime of the material depends on both bulk recombination and surface recombination. Reducing surfacing recombination can lessen the rate at which minority carriers are depleted. The total lifetime of the material includes τ_{rad}, τ_{SRH}, τ_{Aug}, and $\tau_{Surface}$ and

is given by the general equation:

$$\frac{1}{\tau} = \frac{1}{\tau_{rad}} + \frac{1}{\tau_{SRH}} + \frac{1}{\tau_{Aug}} + \frac{1}{\tau_{Surface}} \tag{2.4.1}$$

Eq. (2.4.1) can be written for the low and high injection cases, as demonstrated in the previous subsections. For the low injection case [refer to Eqs. (2.3.5), (2.3.9), and (2.3.19)] the total lifetime can be expressed as:

$$\frac{1}{\tau_{low}} = CN_A + \frac{1}{\tau_{n_0}} + 0 + \frac{1}{\left(\frac{d}{S} + \frac{d^2}{D_n}\right)} \quad \text{for} \quad \Delta n << N_A \tag{2.4.2}$$

Recall that the Auger recombination requires a high injection, so the τ_{Aug} term is zero. Similarly, for the high injection case [refer to Eqs. (2.3.6), (2.3.10), (2.3.15) and (2.3.19)], the total lifetime is:

$$\frac{1}{\tau_{high}} = C\Delta n + \frac{1}{\tau_{n_0} + \tau_{p_0}} + C_{Aug}\Delta n^2 + \frac{1}{\left(\frac{d}{S} + \frac{d^2}{D_n}\right)} \quad \text{for} \quad \Delta n >> N_A \tag{2.4.3}$$

2.5 Temperature Dependent Parameters

The exponential temperature dependence (T) is inherent in the carrier concentration solutions (number densities of electrons and holes, n and p respectively) [28]. However, temperature dependencies for other parameters must be manually incorporated into the model and they are specific to the material. Approximate temperature-dependent expressions for the effective density of states in the conduction band ($N_C(T)$) and valence band ($N_V(T)$) are as follows:

$$N_C = N_{C0}\left(\frac{T}{T_0}\right)^{3/2} \qquad \text{where} \qquad N_{C0} = 2\left(\frac{m_e^* k T_0}{2\pi\hbar}\right)^{3/2} \tag{2.5.1}$$

$$N_V = N_{V0}\left(\frac{T}{T_0}\right)^{3/2} \qquad \text{where} \qquad N_{V0} = 2\left(\frac{m_h^* k T_0}{2\pi\hbar}\right)^{3/2} \tag{2.5.2}$$

T_0 is the reference temperature set to 300 K, m_e^* and m_h^* are the effective electron and hole masses, and $\hbar$ is Planck's constant. The thermal velocity function is given by:

$$v_{th} = v_{th0}\sqrt{T/T_0}, \tag{2.5.3}$$

where v_{th0} is the reference thermal velocity at the reference temperature (T_0) and is given by $v_{th0} = \sqrt{3kT_0/m^*} \approx 10^7$ cm/s. Nonlinearities in $V_{oc}(T)$ are often observed, especially at low temperatures. If $V_{oc}(T)$ remains linear over that range, then nonlinearities due to other temperature dependencies are reduced and, to a first approximation, the measured E_a closely represents the true V_{oc} activation energy for V_{oc} [29]. However, if nonlinearity is observed at operating temperatures, the y-intercept can significantly underestimate the actual activation energy.

2.6 Band Offset at Heterojunctions

At semiconductor heterojunctions, there is a discontinuity in the band structures, giving rise to an offset in the band. Band offset refers to the energy difference between the valence band edge (E_V) and the conduction band edge (E_C) of two different materials or regions in a semiconductor device. This offset plays a crucial role in determining the behavior of charge carriers at interfaces and heterojunctions and can be in the valence band (VBO) and/or in the conduction band (CBO). As an example, consider a heterojunction between material 1 and material 2 (refer to Fig. 2.3). The CBO and VBO are determined by intrinsic material properties such as the electron affinity (χ), and work function (ϕ). The electron affinity refers to the energy level difference between the vacuum level and the bottom of the conduction band, while the work function refers to the minimum amount of energy required to remove an electron from the Fermi level (E_F) of a material to a point just outside the material (i.e., to vacuum) [31]. The CBO is given by Anderson's rule [32]:

$$\text{CBO} = \chi_2 - \chi_1 \tag{2.6.1}$$

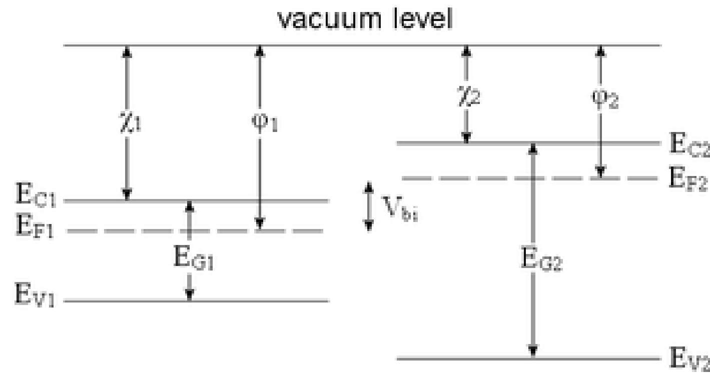

Figure 2.3 Conduction Band Offset (CBO) and Valence Band Offset (VBO) at a Type I hetero-junction of two different materials in a semiconductor device - determined by intrinsic material properties [30].

Similarly, the VBO is given by:

$$\text{VBO} = (\chi_1 + E_{g1}) - (\chi_2 + E_{g2}) \tag{2.6.2}$$

If the valence band edge of one material is higher, it creates a valence band spike at the interface, causing holes to accumulate there (see Fig. 2.3). Conversely, if the valence band edge of one material is lower, it results in a valence band drop, causing electrons to accumulate. Similarly, a negative conduction band offset (conduction band at lower energy) causes electrons to accumulate at the site, and vice versa.

Understanding and controlling these band offsets are crucial for designing semiconductor devices with desirable electronic properties, such as efficient charge carrier transport and reduced recombination losses. Favorable band alignment can facilitate efficient charge transport. Conversely, unfavorable band alignment may result in carrier trapping and recombination, reducing efficiency.

2.7 Activation Energy

The activation energy of solar cells relates to the probability of electrons transitioning from the valence band to the conduction band, which can occur thermally. This thermal generation is described by an exponential relationship: $G_{th} \propto \exp(-E_g/kT)$, E_g being the band

gap and kT the thermal energy. Consequently, the activation energy is approximately equal to the band gap for this process. At the open-circuit voltage (V_{oc}), the reverse current J_L is observed. Applying a voltage reduces the barrier, enabling electrons to flow in a forward current. The activation energy E_a plays a crucial role in determining carrier transport properties and device performance. Activation energy generally refers to the energy barrier that carriers (electrons or holes) must overcome to participate in conduction or recombination processes within the semiconductor material. For optimal current generation, minimal recombination, and higher efficiency, materials with appropriate E_a values are chosen. Higher activation energies can increase the efficiency of a device by lowering recombination rates, but they may also indicate deeper defect states that can trap carriers, leading to non-radiative recombination and reduced device performance. A very delicate balance is required to achieve a higher overall efficiency.

The dominant recombination pathway determines the activation energy, which is why it is vital to delineate where and why recombination occurs in certain parts of the device. In the bulk of the device, the recombination mechanisms lead to an activation energy that is typically equal to the absorber band gap [29]. At an interface, E_a may be equal to the interface band gap, i.e., E_a = $E_{g,i}$ if the interface band gap is less than the absorber bandgap. The CBO at a heterojunction can be calculated: CBO = $E_{g,i}$ - E_g, giving a negative CBO.

CHAPTER 3 METHODOLOGY

3.1 NREL Cd(Se,Te) Devices

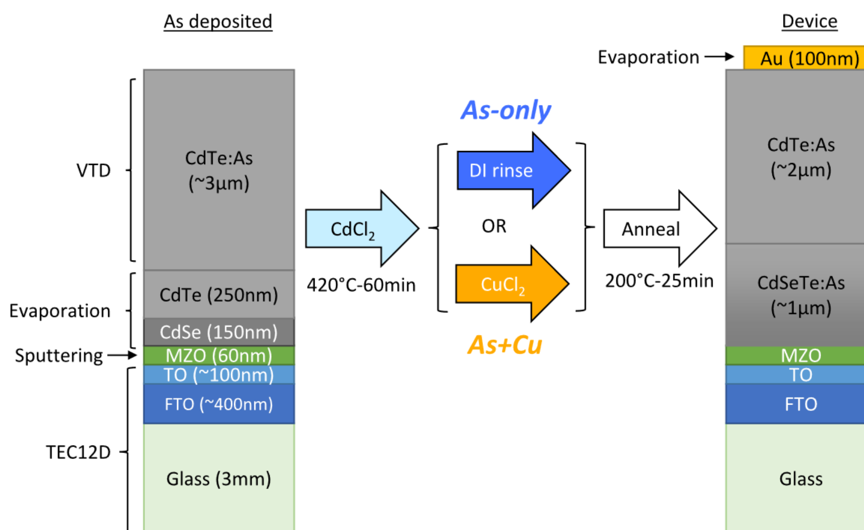

Figure 3.1 As deposited material stack and processing leading to the completed superstrate configuration As-doped Cd(Se,Te) device stack. Left: Stack before $CdCl_2$ treatment. Right: Completed As-doped Cd(Se,Te) device with glass substrate, FTO, MZO layer, Cd(Se,Te) absorber layer, and a back contact [16].

The Cd(Se,Te) device that was modeled is *almost* identical to the device described by E. Colegrove et al [16]. Cd(Se,Te) PV device stacks were fabricated at NREL using a superstrate configuration, as shown in Fig. 3.1 on commercial transparent conducting oxide (TCO) coated glass – NSG TEC™12D. This glass substrate is made of a 3 mm soda-lime glass with approximately 400 nm fluorine-doped tin oxide (SnO_2:F = FTO) and 100 nm of intrinsic tin oxide (i-SnO_2) after which 60 nm of magnesium zinc oxide ($Mg_xZn_{(1-x)}O$ = MZO) was sputtered from 4% (by weight) Mg to Zn target. The simulations in this thesis did not incorporate the MZO layer because newer NREL devices do not include it. Subsequently, 150 nm of cadmium selenide (CdSe) and 250 nm of cadmium telluride (CdTe) were evaporated onto the substrate at a temperature of 450°C. These films were then transferred to a custom-built vapor transport deposition (VTD) system for the deposition of 2–4 μm of arsenic-doped cadmium telluride (CdTe:As). VTD sources consisted of powders prepared from high-pressure Bridgman (HPB) meltgrown, As-doped CdTe boules from Washington State University [33], and mixtures of

cadmium arsenide (Cd_3As_2) and CdTe powders from Materion and 5 N Plus respectively (powders are mixed by weight % with a larger fraction of CdTe).

Vapor-type $CdCl_2$ treatments were conducted in a close-space sublimation system by suspending absorber stacks over $CdCl_2$-coated glass source plates. The $CdCl_2$ treatment was performed at 420°C for 60 min. After the $CdCl_2$ treatment, As-only devices and As + Cu devices were processed a little differently. The As-only devices received a short deionized (DI) water rinse followed by an anneal in the air at 200°C for 25 min in a tube furnace. The As + Cu devices were immersed in a 0.1 mM $CuCl_2$ solution in DI water for 3 min followed by a brief rinse in DI water before receiving the same air anneal process. A 100 nm layer of gold (Au) was then deposited via evaporation through a shadow mask to produce 5 × 5 mm (0.25 cm^2) device pads. Finally, to expose the buried TCO, the absorber was mechanically scraped and then the devices were completed by applying an indium bus bar with an ultrasonic soldering iron.

The experimental data for two devices - V401 and V617, sourced from NREL, were provided to us for analysis. The two primary differences between the devices are that V401 has an MZO layer while V617 does not, and V617 has a Cd(Se,Te) layer with 30% Se and 70% Te, while V401 has a simple CdSe layer before processing. V401 was treated with $CdCl_2$ at 420°C while V617 was treated at 450°C, both for 60 minutes. Table 3.1 depicts the differences between the two devices. Variations in structure and processing yield differences in Se profiles as seen

Device V401	MZO(60nm)	CdSe(150nm)	CdTe(250nm)	CdTe:As(~2.5um)
Device V617		$CdSe_{0.3}Te_{0.7}$(500nm)	CdTe(250nm)	CdTe:As(~2.5um)

Table 3.1 Structural differences in V401 and V617

from Secondary Ion Mass Spectrometry (SIMS) profiles in Fig. 3.2. The “raw counts Se” on the y-axis specifically refer to the number of selenium secondary ions detected under the process of SIMS. Higher counts indicate higher concentrations of selenium in that particular region. Note that the values for the y-axis for device V401 are on the right in orange and that for device V617 are on the left in blue. Device V401 has most of its Se distributed closer to the oxide interface (between 0 and 1 μm) and the raw counts Se asymptotically approaches zero when the depth from

the oxide exceeds $\approx 1.5\ \mu$m. Device V617 has more Se distributed throughout the device and approaches zero when the depth from the oxide exceeds $\approx 3\ \mu$m. The proximity of selenium to the oxide interface can influence the quality of the interface, including the recombination trap site and hence the overall performance.

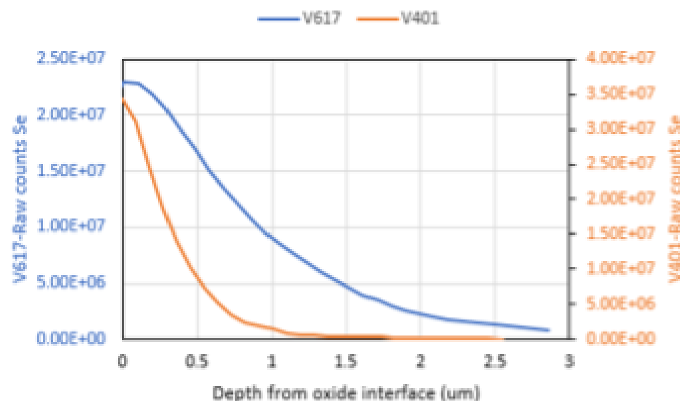

Figure 3.2 Secondary ion mass spectroscopy (SIMS) profiles data of Se profiles for V401 and V617. (Courtesy: NREL)

To compare and characterize the two devices, various quantities can be plotted, such as doping concentration vs. depth, JV curves, and External Quantum Efficiency (EQE). These plots provide a comprehensive understanding of the devices' electrical, optical, and structural properties and performance. This allows us to pinpoint performance-capping factors and assess the impact of fabrication parameters and processes.

Doping concentration vs. depletion width plots give us insight into the spatial distribution of the doping profile while aiding strategies for better charge transport. The differences in the curves indicate varying material properties and/or processing conditions between the devices. In Fig. 3.3, the red curve for device V617 indicates a higher concentration of p-type doping distributed closer to the surface of the material compared to device V401, which has a lower doping density deeper in the material. The higher doping in V617 may result in improved charge transport and collection efficiency near the interface.

Quantum efficiency (QE) is the ratio of the number of carriers collected by the solar cell to the number of photons of a given energy or wavelength incident on the solar cell. The external

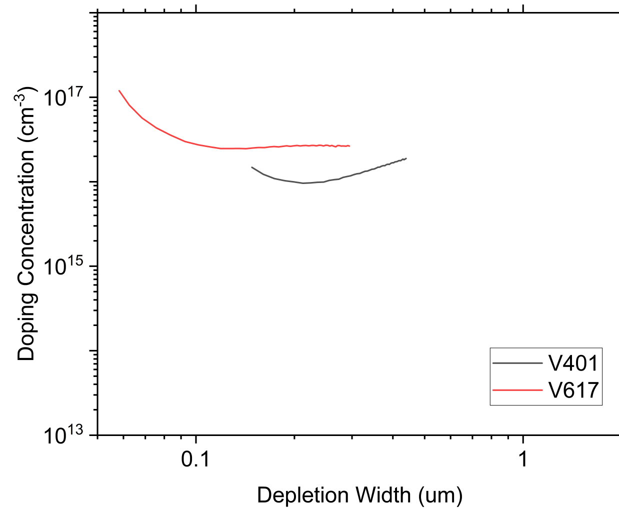

Figure 3.3 Carrier concentration vs. depletion width for NREL Devices V401 and V617 obtained from capacitance vs. voltage measurements

quantum efficiency (EQE) takes optical losses (reflection, transmission) into account, and the internal quantum efficiency (IQE) sheds light on the efficiency with which photons (not reflected or transmitted) can generate carriers that can be collected. The QE broadly offers insight into the device's spectral response and performance across different wavelengths of light and helps identify absorption losses and their location in the device. Fig. 3.4 depicts that device V617 has a better EQE than V401. The plot suggests that device V617 is more efficient in converting photons into current at lower wavelengths ($\lambda = 300 - 500$ nm), while they have a similar efficiency at higher wavelengths ($\lambda > 750$ nm). V617 has no MZO layer which may cause parasitic absorption of photons with $\lambda < 400$ nm, as shown by the higher EQE for lower wavelength values in Fig. 3.4.

Current-voltage (JV) curves provide insight into the electrical behavior and performance of the solar cell under different operating conditions. The most vital function is that it helps in assessing key parameters such as V_{oc}, J_{sc}, FF, and overall efficiency, η. The point at which the current is zero is the V_{oc} and the point at which the voltage is zero is the J_{sc}. Fig. 3.5 shows that for V401, the V_{oc} = 0.65 V and J_{sc} = -26.41 mA/cm^2, while for V617, the V_{oc} = 0.75 V and J_{sc} = -29.45 mA/cm^2. The FF for V401 is 72, while for V617 the FF is 72.9, and the overall efficiency

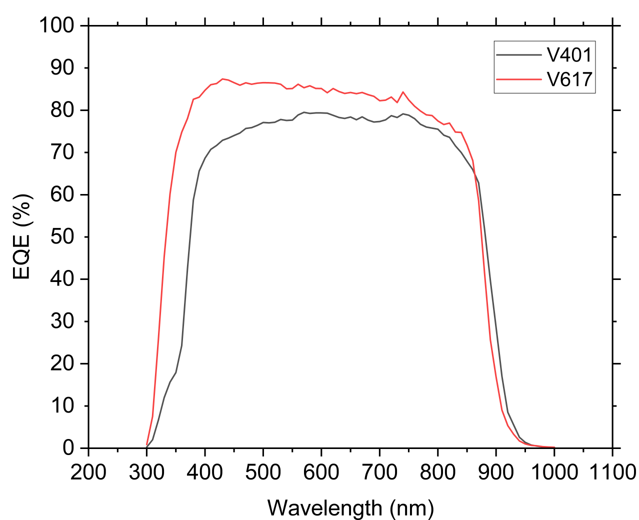

Figure 3.4 External Quantum Efficiency for NREL Devices V401 and V617 indicating that device V617 has a higher overall EQE for a range of incident light wavelengths, especially between $\lambda = 300 - 500$ nm

for the devices is 12.2% and 15.9% for V401 and V617 respectively.

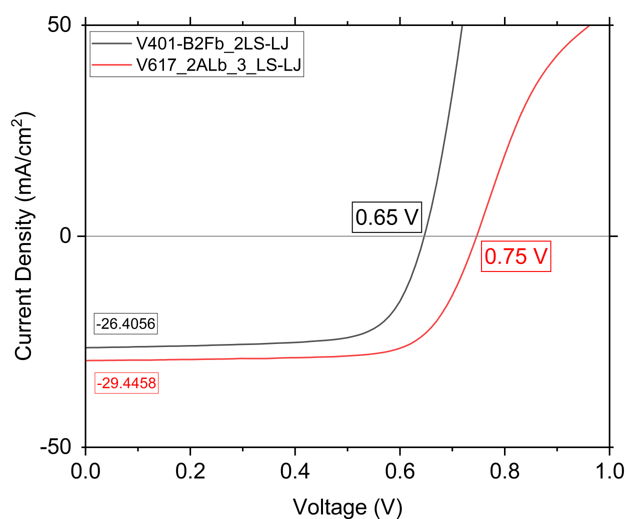

Figure 3.5 JV Curve for NREL Devices V401 and V617. Device V401: V_{oc} = 0.65 V; J_{sc} = -26.41 mA/cm^2; FF = 72; η = 12.2%. Device V617: V_{oc} = 0.75 V; J_{sc} = -29.45 mA/cm^2; FF = 72.9; η = 15.9%.

3.2 Device Simulation

COMSOL Multiphysics [34] is a finite element method simulation software package for various physics and engineering applications, especially coupled phenomena and multiphysics. The software facilitates conventional physics-based user interfaces and coupled systems of partial differential equations. The semiconductor model in COMSOL comprises several components that collectively illuminate the operation of the solar cell. These components include *Definitions*, which detail properties such as the incident light spectrum, selenium grading, bandgap function, electron affinity function, and absorption function for different materials within the device. Additionally, the geometry of the device is specified which builds and integrates it. Within the

Bulk Parameter	Symbol	Unit	SnO_2:F (TCO)	SnO_2 (Buffer)	Cd(Se,Te)	ZnTe:Cu
Thickness	d	μm	0.3	0.05	3.0	0.5
Band Gap	E_g	eV	3.6	3.6	Graded 1.5 - 1.4	2.3
Electron Affinity	χ	eV	4.5	4.5	Graded 4.4 - 4.8	3.14
Relative permittivity (Dielectric)	ε_r		12.2	10.2	10.2	10
Effective DOS, conduction band	N_C	cm^{-3}	2.2×10^{18}	2.2×10^{18}	8.0×10^{17}	8.0×10^{17}
Effective DOS, valence band	N_V	cm^{-3}	1.8×10^{19}	1.8×10^{19}	1.8×10^{19}	1.8×10^{19}
Electron & Hole Thermal velocity	v_{th}	cm s^{-1}	1.0×10^{7}	1.0×10^{7}	1.0×10^{7}	1.0×10^{7}
Mobility, electron	μ_n	$cm^2V^{-1}s^{-1}$	100	100	320	50
Mobility, hole	μ_p	$cm^2V^{-1}s^{-1}$	25	25	40	50
Shallow Acceptor Density	N_A	cm^{-3}			1.0×10^{16}	1.0×10^{16}
Shallow Donor density	N_D	cm^{-3}	1.0×10^{19}	1.0×10^{17}		

Table 3.2 Cd(Se,Te) device parameters for COMSOL set-up. Layers include a SnO_2:F TCO, a SnO_2 buffer layer, the Cd(Se,Te) absorber layer, and a ZnTe:Cu back contact [35].

Semiconductor module, comprehensive equations elucidate the mathematical operations of the device. This encompasses a range of partial differential equations defined in Chapter 2 and

addresses the mechanics of doping as well as the various types of recombination occurring at each layer and heterojunction within the device. A baseline device model for the Cd(Se,Te) cell, resembling the NREL device V617, was created with various parameters and properties listed in Table 3.2.

Fig. 3.6 is a snapshot of the Cd(Se,Te) device with an SnO_2:F TCO Layer, SnO_2 Buffer Layer, Cd(Se,Te) Absorber Layer, and ZnTe:Cu Back Contact Interface.

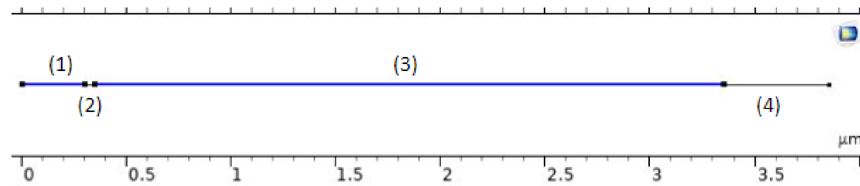

Figure 3.6 Cd(Se,Te) Device: (1) SnO_2:F TCO Layer (2) SnO_2 Buffer Layer (3) Cd(Se,Te) Absorber Layer (4) ZnTe:Cu Back Contact Interface

- The selenium concentration in this device setup is graded and is given by the function:

$$Se(x) = C_0 \left[1 - \text{erf}\left(\frac{x - (W_{TCO} + W_{Buffer})}{L}\right)\right] \tag{3.2.1}$$

where x is the depth into the device and C_0 is the maximum selenium alloy fraction which is set to 0.3 (recall that our model is Cd($Se_{0.3}$,$Te_{0.7}$)). W indicates the width (of the TCO

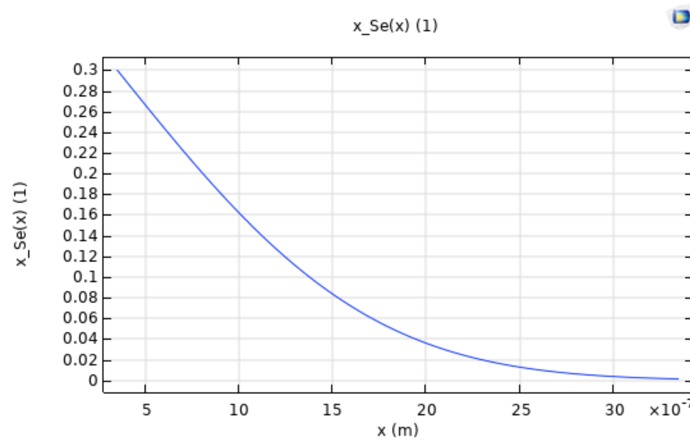

Figure 3.7 Selenium grading as a function of depth into the device x. The y-axis is the selenium alloy fraction, with a maximum of 30% Se in the Cd(Se,Te) absorber layer.

and buffer), erf is the error function given by $\mathrm{erf}(x) = \frac{2}{\sqrt{\pi}} \int_0^x e^{-t^2}\, dt$, and L is the selenium diffusion length which is set to 1.5 μm. Fig. 3.7 from COMSOL shows the selenium grading as a function of depth (x) where the y-axis is the selenium alloy fraction. Selenium grading helps tailor the bandgap profile by minimizing the formation of defects and dangling bonds which are popular recombination sites.

- The bandgap of the Cd(Se,Te) layer is given by the function:

$$E_g(y)_{Cd(Se,Te)} = 1.5(1-y) + 1.7y - 0.8y(1-y) \tag{3.2.2}$$

Note that the variable y here is the Se alloy fraction of the Cd(Se,Te) absorber layer, with a maximum of y = 1. Fig. 3.8 from COMSOL shows the bandgap of Cd(Se,Te) in units of eV as a function of the Se fraction, y. The Se grading profile is given by Eq. 3.2.1, which makes the bandgap a function of $E_g[Se(x)]$. For instance, for 20% selenium content, the bandgap of the absorber is ≈ 1.41 eV.

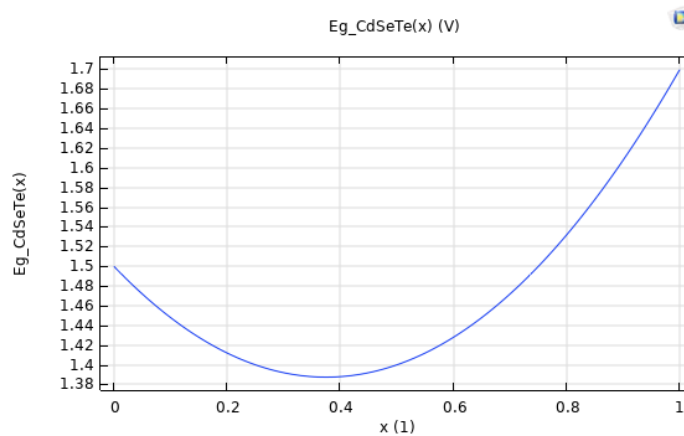

Figure 3.8 Bandgap function $E_g(y)$ in eV for Cd(Se,Te), with the x-axis as the Se fraction in the Cd(Se,Te) absorber layer. The bandgap is graded between ≈ 1.4 and 1.5 eV throughout the Cd(Se,Te) absorber layer.

- The work function (ϕ) and electron affinity (χ) defined in Chapter 2 are essential in understanding and studying the conduction and valence band offsets in semiconductor

devices, and hence their efficiencies. The electron affinity is given by the function:

$$\chi_{Cd(Se,Te)}(y) = 4.4(1-y) + 4.75y + 0.4305y(1-y) \tag{3.2.3}$$

Fig. 3.9 shows the electron affinity in eV as a function of the Se fraction of the absorber layer. If the selenium content is at 30%, as in the simulations carried out for this thesis, then the $\chi \approx 4.59$ eV. The χ for this device goes from ≈ 4.40 to 4.6 eV throughout the Cd(Se,Te) absorber layer, assuming that the maximum selenium alloy fraction is 0.3.

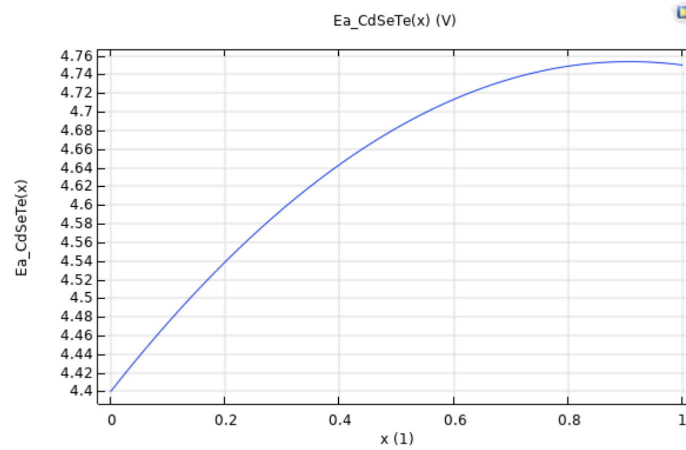

Figure 3.9 Electron affinity function $\chi(y)$ for Cd(Se,Te), with the x-axis as the Se fraction in the Cd(Se,Te) absorber layer. The electron affinity goes from ≈ 4.40 to 4.60 eV throughout the Cd(Se,Te) absorber layer.

- The bandgap grading $E_g(x)$ as a function of the depth x into the device is given in Fig. 3.10, showing the variation in the bandgap throughout the device. The E_g ranges from ≈ 1.4 - 1.5 eV throughout the device. For instance, at a depth of 2 μm, the bandgap is 1.48 eV.

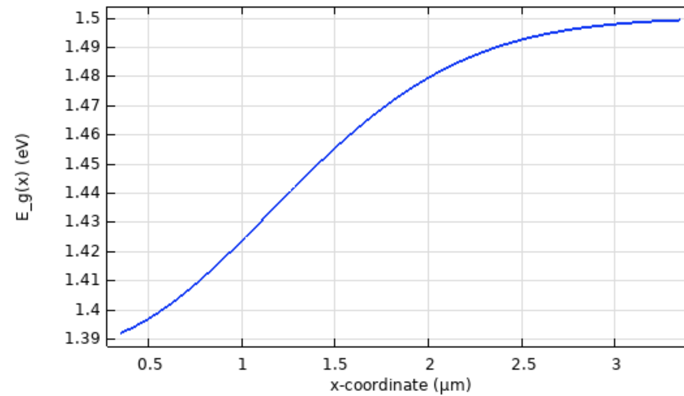

Figure 3.10 Bandgap energy as a function of the device depth, x coordinate. The E_g ranges from $\approx$ 1.4 - 1.5 eV throughout the device.

3.2.1 Parameter Space

COMSOL enables the execution of a *Study*, allowing for the analysis of various parameter ranges such as temperature, electron and hole recombination velocities, and light intensities. These *Studies* conduct a parametric sweep across the specified parameter range. The simulations of this work are categorized into two main sections - Se-graded devices (See Fig. 3.7) and Uniform Se devices (or Uniterns), with the outcomes presented in Chapter 4. The first section comprises JVTi studies (i) with the SnO_2 buffer layer and (ii) without the SnO_2 buffer. For the case without the buffer layer, (iii) the back contact effects, and (iv) the incorporation of a new back contact ZnTe:Cu interface were investigated. The second section studies (v) the uniform Se device models, also known as Uniterns, and is compared to the Se-graded devices. Below are the specific COMSOL parameters assigned to each setup, encompassing the five (i-v) parameter sets:

i. For the **Se-graded device model with the SnO_2 buffer layer** the parameter space is given in Table 3.3. Note that 1 Sun = 100 mW/cm^2 light intensity. In order to study the front surface and bulk recombination, the back surface recombination velocity was constant, set to $S_b = 10^5$ cm/s. The simulations solve for voltages up to 1.2 V, with a voltage step of 0.03 or 0.02 V. The SnO_2 buffer layer has a bandgap of 3.75 eV and a relative permittivity χ of 10.2.

Parameter Name, Symbol	Range	Step Size
Front surface recombination velocity, S_f	10 – 10^7 cm/s	x10
Bulk minority carrier lifetime, τ	0.1 – 1000 ns	x10
Conduction Band Offset, CBO	–0.4 to 0.2 eV	0.2 eV
Temperature, T	225 – 350 K	25 K
Light intensity, i	0.001 – 1 Sun	x10

Table 3.3 Parameter space for Se-graded device model with buffer layer

ii. For the **Se-graded device model without the SnO_2 buffer layer** the parameter space is given in Table 3.4. To study how much the buffer layer/TCO affects the device, the buffer

Parameter Name, Symbol	Range	Step Size
Front surface recombination velocity, S_f	10 – 10^7 cm/s	x10
Bulk minority carrier lifetime, τ	0.1 – 1000 ns	x10
Conduction Band Offset, CBO	–0.2 eV	
Temperature, T	225 – 350 K	25 K
Light intensity, i	0.001 – 1 Sun	x10

Table 3.4 Parameter space for Se-graded device model without buffer layer

layer (aka ESC: Electron Selective Contact) was replaced with a TCO (Transparent Conducting Oxide). The buffer layer is identical to the TCO, except for its doping level. The TCO doping is 10^{19} cm^{-3} n-type and the TCO that replaces the buffer layer is doped 10^{17} cm^{-3} n-type. Note that the SnO_2 buffer layer in Table 3.2 lists the values for the case when the buffer layer has been replaced by the TCO, which is why the parameters of the TCO and buffer layer are the same except the thickness and doping level.

iii. For the **back contact of the Se-graded device model without the SnO_2 buffer layer** the parameter space of the simulations is given in Table 3.5. The back contact in solar cells completes the electrical circuit to extract the generated electrical current. It helps to efficiently collect and transport the electrons and holes, contributing to the overall performance of the device. To study the back contact and the recombination that occurs, the back surface recombination velocity S_b was varied, while keeping the front surface recombination constant, set to $S_f = 100$ cm/s. The light intensity is set at 1 Sun, and to neglect the effects of the CBO, it was set to zero. The flow of holes from the circuit into the

Parameter Name, Symbol	Range
Back surface recombination velocity, S_b	$10^5, 10^6, 10^7$ cm/s
Back barrier for holes, Φ_{bp}	0.2 & 0.4 eV
Bulk minority carrier lifetime, τ	1000 ns
Temperature, T	225 - 350 K

Table 3.5 Parameter space for back contact study: Se-graded device model without buffer layer

device also depends on the potential barrier at the back contact, Φ_{bp}, or the *Schottky barrier*, as depicted in Fig. 3.11. For optimal current flow, Φ_{bp} should be as small as possible and voltage-independent. The effect of the Φ_{bp} was simulated and analyzed.

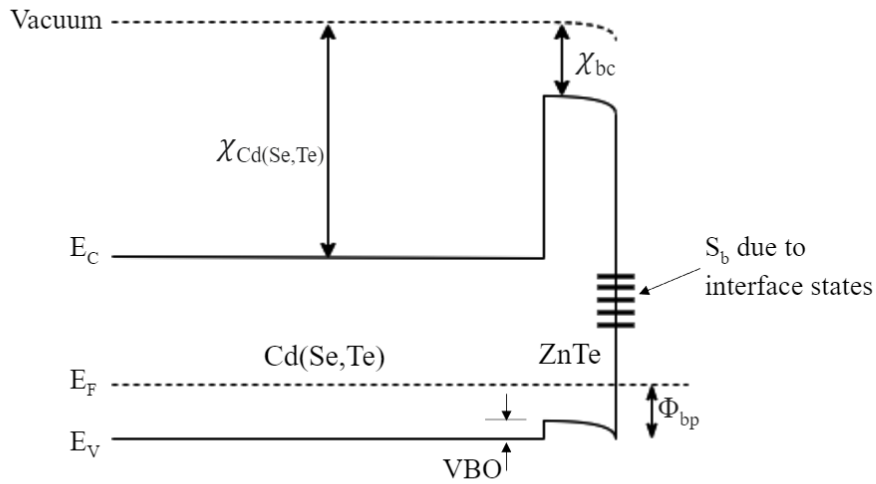

Figure 3.11 Energy band diagram showing the electron affinity χ for Cd(Se,Te) and the ZnTe back contact, and the valence band offset (VBO) at the Cd(Se,Te)/ZnTe interface. The back barrier to holes, Φ_{bp} is the Schottky barrier, which needs to be as small as possible for optimal current flow.

iv. For the **new back contact interface of the Se-graded device model without the SnO_2 buffer layer** the parameter space of the simulations is given in Table 3.6. ZnTe, an important and environmentally friendly material, is a II-VI group compound semiconductor with a wide direct band gap of 2.26 eV and a low electron affinity of 3.53 eV [36]. In commercial thin-film CdTe solar cells, Cu-doped ZnTe:Cu serves as the hole-selective back contact. However, ZnTe:Cu does not effectively passivate the back interface or provide the desired electron reflection to enhance device performance [17]. The diffusion of Cu ions, including those in ZnTe:Cu, into CdTe leads to the formation of shallow acceptor states

(resulting in p-type doping). Nevertheless, achieving loss-free, electron-reflecting, and hole-transporting layers that form Ohmic contacts remains a significant materials challenge. The efficiency of hole transport from CdTe into the back contact, and consequently the overall solar cell performance, is greatly influenced by the valence band alignment. A layer

Parameter Name, Symbol	**Range**
Valence band offset, VBO	-0.4 to 0.2 eV
Back barrier for holes, Φ_{bp}	0.2 & 0.4 eV
Back surface recombination velocity, S_b	$10^5, 10^6, 10^7$ cm/s
Bulk minority carrier lifetime, τ	1000 ns
Temperature, T	225 – 350 K

Table 3.6 Parameter space for new back contact interface: Se-graded device without buffer layer

of ZnTe:Cu was incorporated into the simulation, with a thickness of 500 nm, $E_g = 2.30$ eV, and χ = 3.14 eV. The light intensity was set to 1 Sun, and $S_f = 100$ cm/s. The back contact doping was 10^{18} cm^{-3} p-type and the back contact electron and hole mobilities were both 50 cm^2/Vs. The valence band offset (VBO) at the Cd(Se,Te)/ZnTe:Cu interface was varied and the CBO at the Cd(Se,Te)/SnO_2 interface was set to zero. To incorporate the Valence Band Offset as a parameter to COMSOL, Eq. (3.2.4) was derived and input for the electron affinity for the back contact χ_{bc}:

$$\chi_{bc} = \chi_{Cd(Se,Te)} + E_{g,Cd(Se,Te)} - E_{g,bc} + VBO \tag{3.2.4}$$

where $\chi_{Cd(Se,Te)}$ is the electron affinity for the absorber layer Cd(Se,Te), $E_{g,Cd(Se,Te)}$ is the bandgap for Cd(Se,Te), and $E_{g,bc}$ is the bandgap at the back contact [see Eq. 2.6.2].

v. For the **uniform Se-graded device model with the SnO_2 buffer layer** the parameter space of the simulations is given in Table 3.7. Unitern devices were simulated to study the effect of graded vs. uniform selenium concentration in Cd(Se,Te) thin film. Initial device models were graded with selenium (see Fig. 3.7), whereas the Uniterns have a constant Se composition throughout the device. There were three cases of selenium compositions with and without arsenic doping:

Parameter Name, Symbol	**Range**
Front surface recombination velocity, S$_f$	$10^2, 10^3, 10^4$ cm/s
Bulk minority carrier lifetime, τ	1 ns
Temperature, T	-213 to 333 K

Table 3.7 Parameter space for Uniterns: Uniform Se device without buffer layer

- 0% Se with $E_g = 1.5$ eV. Two cases: One with 0% As doping (p-type 10^{14} cm^{-3}) and another with 1% As doping (p-type 10^{15} cm^{-3}).
- 20% Se with $E_g = 1.41$ eV and 2×10^{16} cm^{-3} p-type doping
- 40% Se with $E_g = 1.36$ eV and 8×10^{15} cm^{-3} p-type doping

The above compositions were selected based on available data from collaborators. The simulations had the light intensity set to 1 sun with a CBO = -0.2 eV and S$_b = 10^5$ cm/s.

3.2.2 JVTi Methodology

JVTi data at NREL is collected using a current-voltage source/meter (Agilent B2912A) connected to the sample contacts in a 2-wire configuration when the sample is mounted in a closed-cycle helium cryostat. Although absolute currents are small, some series resistance effects may occur. Temperature T is swept through the desired range using a Lakeshore 331 temperature controller that stabilizes the temperature to within one degree Celsius. An automated data collection program maintains the stabilized temperature for a controlled time frame (1 to 5 minutes) before collecting the JV data. Due to conductive cooling and heating through the glass, there are temperature offsets between the cold-finger stage and the sample, so the device temperature is recorded using a secondary sensor attached directly to the device side of the glass substrate. The sample is illuminated through the cryostat windows and a hole in the cold finger stage with a Xe-bulb-based solar simulator capable of greater than 1-sun intensity. Multiple intensity levels of the solar-simulated light can be selected with automated neutral-density filters.

The simulations in COMSOL solve the partial differential equations and give details and key parameters such as the V_{oc}, efficiency, average terminal current density, and short circuit current density (J_{sc}). For each combination of parameters, the V_{oc} values from the generated

output were extracted to create V_{oc} vs. T plots. According to Eq.2.1.2, repeated here for convenience:

$$V_{oc} = \frac{E_a}{q} - A\frac{kT}{q} \ln \frac{J_{00}}{J_{sc}} \tag{3.2.5}$$

the y-intercept, i.e., at T = 0 K, gives us the activation energy E_a. A linear fit in Origin Pro gives the E_a values. Note that E_a itself can be a function of temperature as well. Using this equation and extrapolation method, the activation energy can be numerically determined and plotted as a function of the key parameters under investigation, such as the front surface recombination velocity S_f and bulk lifetime τ. See Chapter 4 Results.

CHAPTER 4 RESULTS AND DISCUSSION

The results are divided into five sections: Sections one and two respectively include the results for the Se-graded device with and without an SnO_2 buffer layer, including a back contact study and a study for a new back contact interface. Section three includes Unitern (uniform Se content) devices without an SnO_2 buffer layer. The fourth section compares simulations with experimental data for the Se-graded device with the buffer. The lowercase Roman numerals in Fig. 4.1 correspond to the respective parameter set in Section 3.2.1. A summary of the sections in this chapter is provided below.

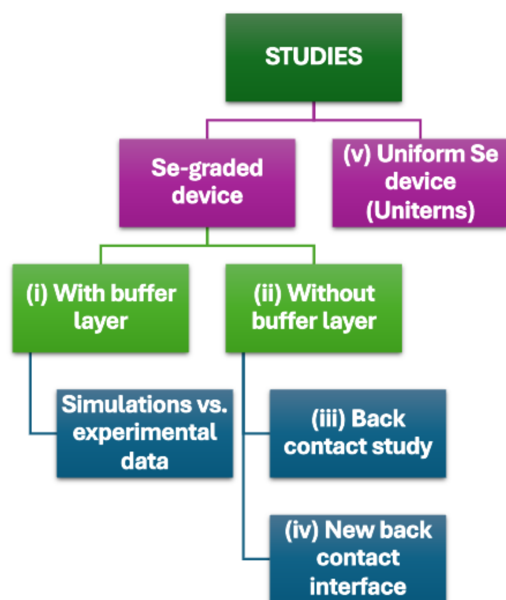

Figure 4.1 Breakdown of the studies reported herein. Roman numerals correspond to the parameter spaces investigated as listed in Section 3.2.1.

Section 4.1 Se-graded Device With Buffer Layer: JVTi Study (i)

Section 4.2 Se-graded Device Without Buffer Layer: JVTi Study (ii)

Section 4.2.1 Back Contact Study (iii)

Section 4.2.2 Incorporation of ZnTe:Cu as Back Contact Interface (iv)

Section 4.3 Uniterns: Uniform Se Device Without Buffer Layer (v)

Section 4.4 Comparison of Simulations and Experimental Data

4.1 Se-graded Device With Buffer Layer: JVTi Study

The simulated device model in this section includes an undoped (intrinsic) SnO_2 buffer layer between the semiconductor and highly doped transparent conducting oxide (TCO, SnO_2:F). After setting up the simulations as described in Section 3.2.1, calculations from COMSOL were extracted and imported into Origin Pro to plot and analyze. The program execution provides key parameters such as the V_{oc} and the short circuit current density (J_{sc}). Fig. 4.2 is an example of a room temperature (T = 300 K) JV plot for a CBO = 0 eV, i = 1 Sun, τ = 1 ns generated on COMSOL. The zoomed-in section of the plot shows the J = 0 intercepts, when no current is flowing, i.e., the open-circuit voltage V_{oc}. Note that for S_f = 10 to 10^3 cm/s, the V_{oc} values all equal 0.823 V. From left to right on the plot, the V_{oc} values increase as the front surface recombination velocity decreases. Here, the J_{sc} ranges from -29.03 to -27.27 mA/cm^2 for S_f = 10 to 10^7 cm/s respectively. By simulating JV curves for every point in the parameter space, V_{oc} vs. temperature plots were generated for all sets of parameters from Table 3.3.

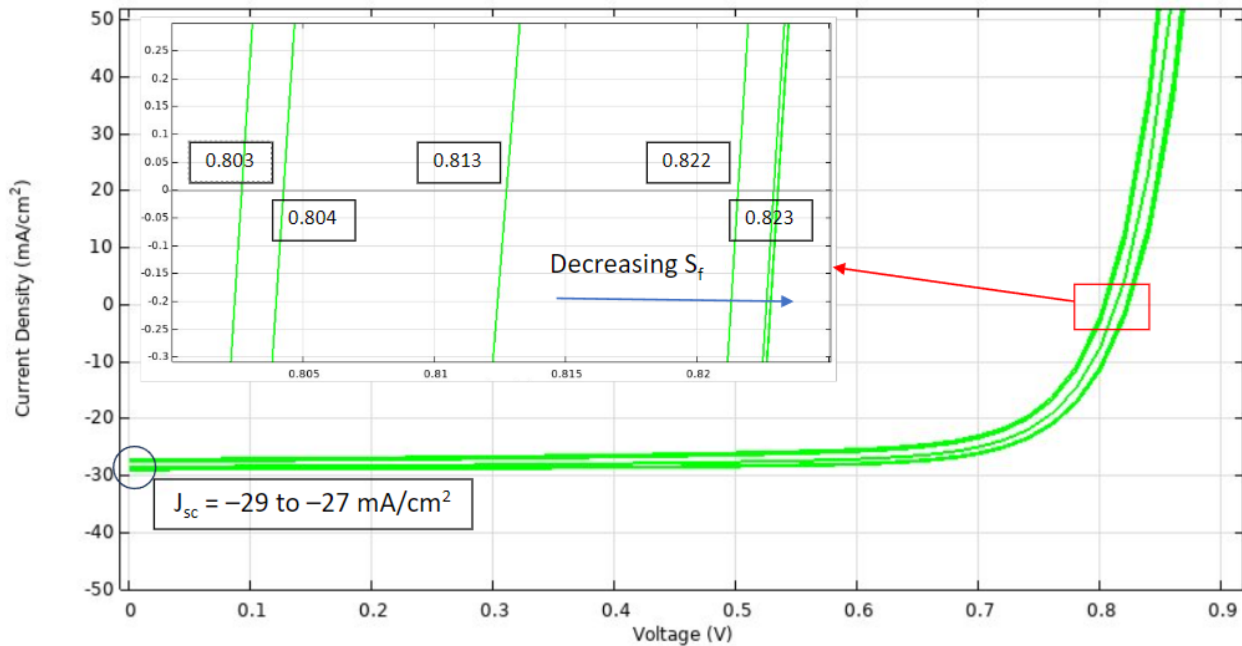

Figure 4.2 Simulated room temperature (T = 300 K) JV curves for Cd(Se,Te) device over a range of front surface recombination velocities. Parameters: i = 1 Sun, CBO = 0 eV, τ = 1 ns, T = 300 K, $S_f = 10$ to 10^7 cm/s. V_{oc} is extracted from the x-intercept (zoomed section) of the JV curve.

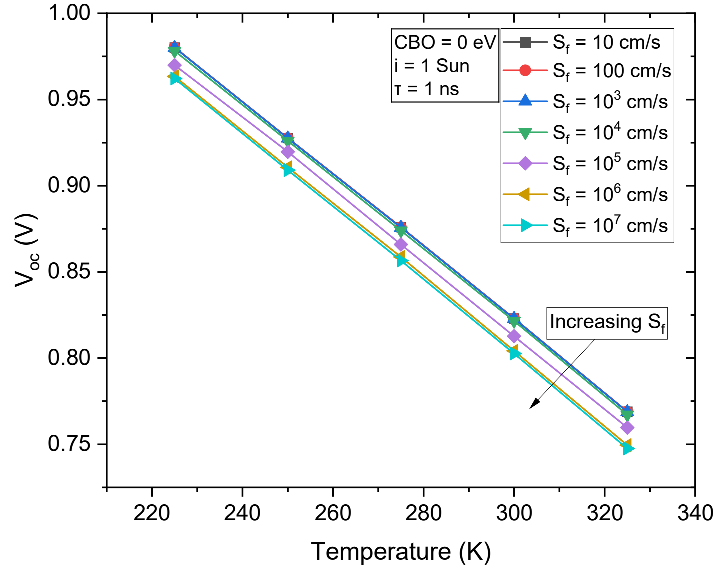

Figure 4.3 V_{oc} vs. T to extract the activation energy E_a from the y-intercept for a range of front surface recombination velocities and CBO = 0 eV, i = 1 Sun, and τ = 1 ns.

The E_a values for each parameter set were extracted from the y-intercept (T = 0 K) of the V_{oc} vs. T plots, as explained in Sections 3.3.1 and using Eq. (2.1.2). As an example, Fig. 4.3 is a V_{oc} vs. T plot for CBO = 0 eV, i = 1 Sun, and τ = 1 ns. Each plot line on it represents one value of S_f, ranging from 10 to 10^7 cm/s. A lower front surface recombination velocity S_f value indicates a slower rate of recombination at the front surface. As expected, due to increased surface recombination, V_{oc} declined as the S_f increased. In this graph, the first four plot lines for S_f are almost perfectly superimposed over each other, indicating that varying the front surface recombination velocity between 10 and 10^4 cm/s does not affect the activation energy significantly. V_{oc} decreases at S_f = 10^5 cm/s, then is unchanging again at S_f = 10^6 and 10^7 cm/s. The E_a values are given in Table 4.1 for each S_f and temperature in this set. Note that the V_{oc} values in Fig. 4.2 are equivalent to V_{oc} values in Table 4.1 for T = 300 K. The collection of V_{oc} vs. T plots generated in this research to extract the E_a values are given in Appendix B:6.

The activation energies in Table 4.1 are over a wide range of S_f, fluctuating slightly but remaining near 1.455 eV for S_f = 10 cm/s to 10^7 cm/s. Note that the linear regression fitting error

S_f (cm/s) $\rightarrow$	10	100	10^3	10^4	10^5	10^6	10^7
Temp (K)	V_{oc} (V)	V_{oc} (V)	V_{oc} (V)	V_{oc} (V)	V_{oc} (V)	V_{oc} (V)	V_{oc} (V)
225	0.980	0.980	0.980	0.978	0.970	0.963	0.962
250	0.928	0.928	0.927	0.926	0.920	0.911	0.909
275	0.876	0.876	0.876	0.874	0.866	0.859	0.857
300	0.823	0.823	0.823	0.822	0.813	0.804	0.803
325	0.769	0.769	0.769	0.767	0.760	0.750	0.748
E_a **(eV)**	**1.455**	**1.455**	**1.455**	**1.453**	**1.446**	**1.445**	**1.445**

Table 4.1 Activation energies for CBO = 0 eV, i = 1 Sun and τ = 1 ns over a range of temperatures and S_f. Note: Row T = 300 K corresponds to the V_{oc} values in Fig. 4.2.

is in the range of $\pm$ 8.57 meV for these E_a values. Also, V_{oc} varies only slightly by about 20 mV over S_f variation of seven orders of magnitude. This suggests that the V_{oc} is governed by bulk processes for these parameter settings, otherwise the V_{oc} would be sensitive to S_f. The reduction of V_{oc} with the temperature in Table 4.1 is approximately -0.27%/K, as expected from normal V_{oc} temperature coefficient for Cd(Se,Te) devices [15].

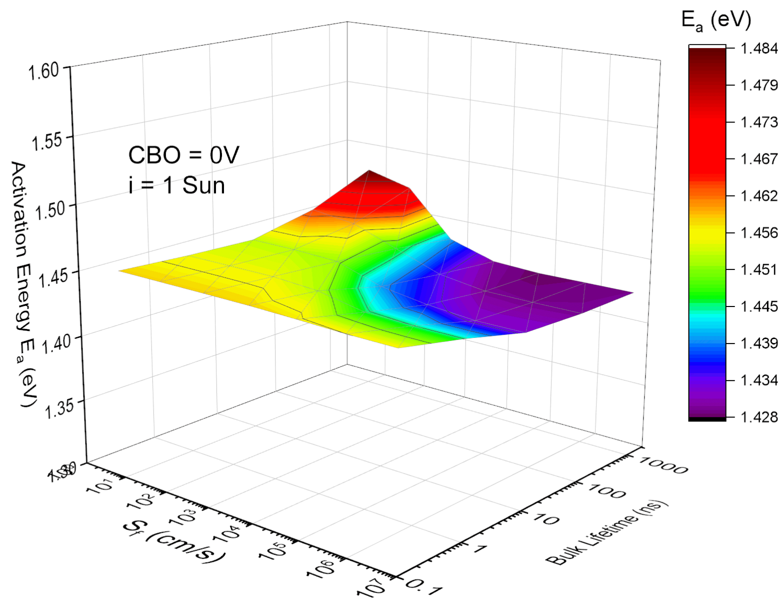

Figure 4.4 E_a vs. τ vs. S_f for CBO = 0 eV and i = 1 Sun. The E_a values were extracted from V_{oc} vs. T plots and varied by 56 meV over the parameter space.

The above results considered only a relatively low bulk lifetime of 1 ns. To visualize the

transition between bulk and interface recombination-dominated regions, 3D plots of E_a as a function of τ and S_f were plotted. An example is shown in Fig. 4.4 which indicates that when CBO = 0, meaning that the front heterojunction interface band gap and bulk Cd(Se,Te) band gap are equal, E_a is relatively insensitive to both S_f and τ. E_a varies by only 56 meV over the parameter space. The overall greatest E_a of 1.484 eV occurs at the lowest S_f = 10 cm/s and highest τ = 1000 ns. For $\tau < 100$ ns, E_a appears to remain relatively flat for low S_f, then decreases for $S_f \approx 10^3$ - 10^5 cm/s, where it plateaus again at a lower value in the range of $E_a \approx$ 1.438 eV. This transition to lower E_a as S_f increases may be due to the graded band gap in these models, which creates a smaller band gap (E_g) near the interface relative to deeper in the bulk (refer to Fig. 3.10). A total of twelve 3D plots were generated for the four CBO and three light intensity values (i = 1, 0.1, 0.01 Sun) (See Table 3.3 and Appendix A:6).

(a) Activation Energy Dependence on CBO: To examine the effect of the CBO (or ΔE_c) on E_a, 3D plots for four CBO values at $i = 1$ Sun were compared. Fig. 4.5 has four color maps,

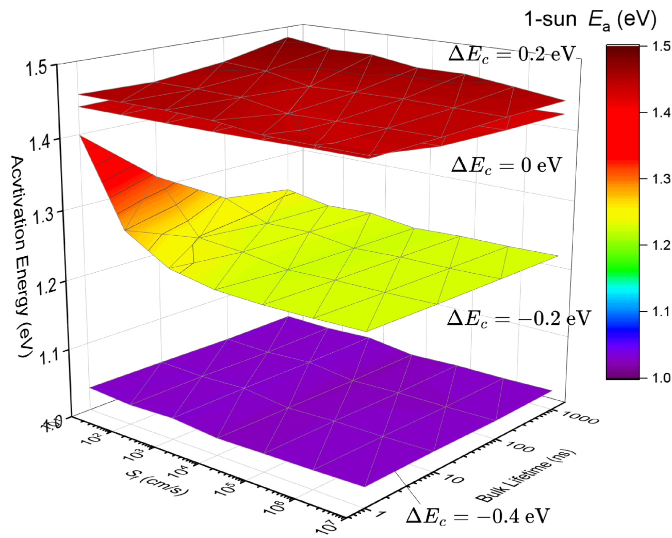

Figure 4.5 E_a vs. τ vs. S_f at i = 1 Sun, for CBO = ΔE_c = -0.4, -0.2, 0, 0.2 eV. At CBO = -0.2 eV, the E_a increases dramatically for $S_f < 10^4$ cm/s and $\tau < 100$ ns). CBO = 0.2, 0, -0.4 eV had minimal variation in the E_a.

each representing one CBO value (CBO = ΔE_c = -0.4, -0.2, 0, 0.2 eV). Between CBO = 0 eV and 0.2 eV, i.e., for positive, or "spike", alignments, there was no significant shift in the E_a and

$E_g \approx E_a$. For large negative cliffs, CBO = -0.4 eV, the E_a can be due to the front interface band gap for all values of S_f and τ. CBO = 0, 0.2, -0.4 eV had small E_a variations. At CBO = -0.2 eV, E_a increases dramatically (see peak in Fig. 4.5) for lower τ and S_f values ($S_f < 10^4$ cm/s and $\tau < 100$ ns), suggesting a transition from front interface to bulk recombination. At higher τ and S_f values, meaning the front surface recombination is most likely dominant, the E_a has minimal variations and remains at E_a = 1.23 eV, which is the magnitude of the interface bandgap when CBO = -0.2 eV.

V_{oc} is directly proportional to E_a [see Eq. (2.1.2)]. E_a, and therefore V_{oc}, tends to be lower when CBO < 0. Fig. 4.6 reinforces that point, showing a decline in V_{oc} as CBO becomes increasingly negative. It is also evident that the trend is independent of light intensity. Those results are for τ = 100 ns and S_f = 10^3 cm/s, but the trend holds as long as S_f and τ are not too low, as shown by the increasing E_a trend in Fig. 4.5. Overall, JVTi characteristics can indicate that front surface recombination is the dominant mechanism when the activation energy is lower than the bulk bandgap ($E_a < E_g$). In that case, CBO < 0 and E_a quantifies the interface band gap ($E_{g,i} < E_g$). The latter provides insight into the band alignment at the front interface.

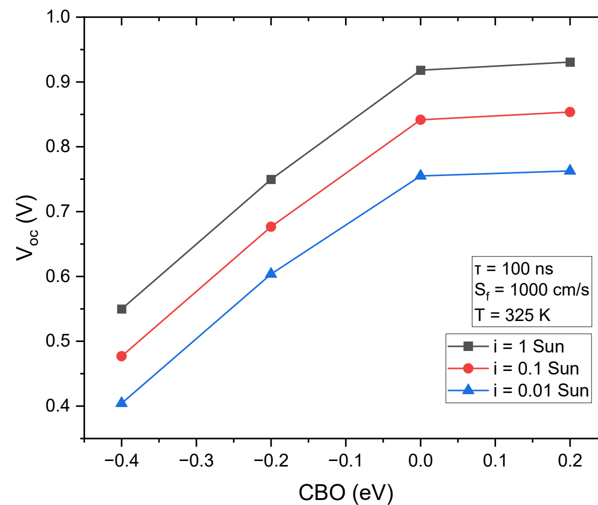

Figure 4.6 V_{oc} vs. CBO at T = 325 K, S_f = 1000 cm/s, τ = 100 ns, and at various light intensities shown in the legend. V_{oc} declines as CBO becomes increasingly negative.

(b) Activation Energy Dependence on Light Intensity: Similarly, to study the effect of the light intensity on the E_a, the light intensity was varied. Fig. 4.7 shows the activation energy as a function of S_f and τ at CBO = -0.2 eV and for light intensities of 0.01, 0.1 and 1 Sun. At higher values of S_f and τ, E_a is insensitive to light intensity. However, E_a increases with light intensity when $S_f < 10^4$ cm/s and $\tau < 100$ ns. These results suggest a shift from front interface recombination (when $S_f \gtrsim 10^3$ cm/s) to bulk recombination at lower light intensity. That shift

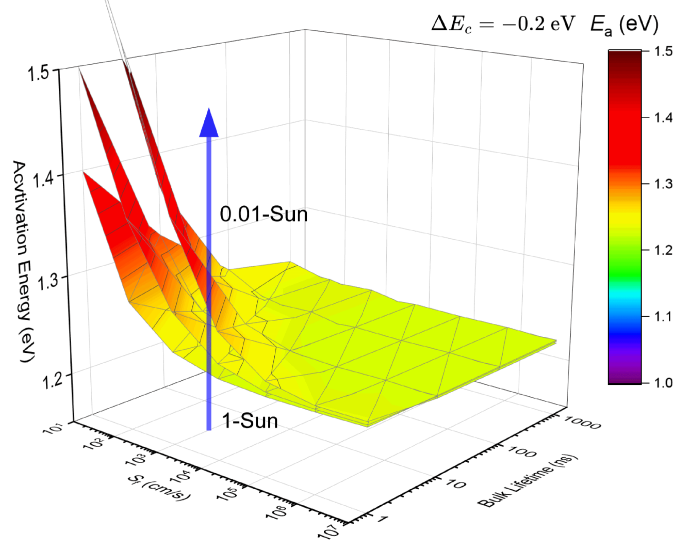

Figure 4.7 E_a vs. τ vs. S_f for i = 1, 0.1, 0.01 Sun at CBO = ΔE_c = -0.2 eV. When $S_f < 10^4$ cm/s and $\tau < 100$ ns, E_a increases with light intensity, suggesting a shift from interface to bulk recombination, and is more significant at lower light intensities.

can be explained by recalling that $E_a \approx E_g$ for bulk recombination and $E_a \approx E_{g,i} < E_g$ for front interface recombination. The trend can be seen more clearly in Fig. 4.8 (a) where E_a is plotted against light intensity at S_f = 10^3 cm/s, CBO = -0.2 eV for various τ. At the lowest value of $\tau = 1$ ns, E_a increases significantly as light intensity decreases.

As Eq. (2.1.2) shows, $V_{oc} \propto \ln(J_L)$ and J_L is directly proportional to intensity. Therefore, V_{oc} increases logarithmically with light intensity, which is exhibited in Fig. 4.8 (b). From there it is clear that V_{oc} decreases as CBO becomes increasingly negative but the logarithmic trend is maintained. For i = 1 Sun, CBO = 0.2 eV and 0 eV yield $V_{oc} \approx$ 0.92 V, where as CBO = -0.2 gives a $V_{oc} \approx$ 0.75 V, and CBO = -0.4 eV gives $V_{oc} \approx$ 0.55 V.

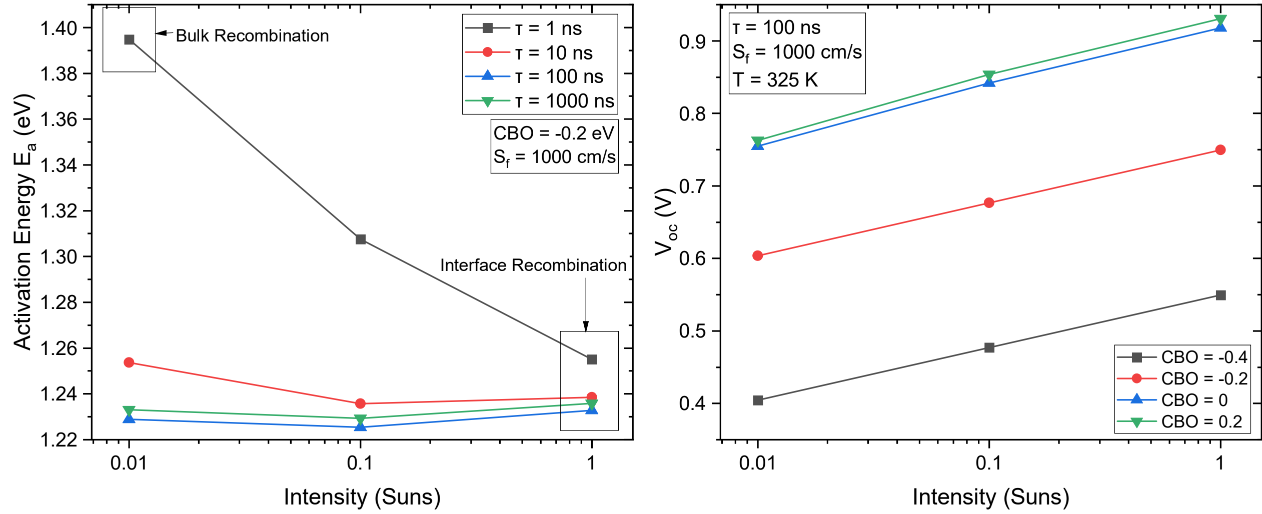

Figure 4.8 (a) E_a vs. light intensity i at CBO = -0.2 eV and S_f = 1000 cm/s for τ = 1 to 10^3 ns. At τ = 1 ns, E_a increases significantly as i decreases, suggesting a shift from interface to bulk recombination (b) V_{oc} vs. light intensity i at T = 325 K, S_f = 1000 cm/s, τ = 100 ns for CBO = -0.4, -0.2, 0, 0.2 eV. V_{oc} decreases as the CBO becomes more negative.

4.2 Se-graded Device Without Buffer Layer: JVTi Study

This section studies the effects of removing the intrinsic SnO_2 buffer layer such that the Cd(Se,Te) is in direct contact with the highly doped TCO layer. Simulations were conducted for the parameter space described in Section 3.2.1 and Table 3.4, and the data were extracted.

Fig. 4.9 is the V_{oc} vs. T plot for CBO = -0.2 eV, 1 Sun intensity and τ = 1 ns. The blue symbols refer to the device model with the buffer layer and the red symbols refer to the device model without the buffer layer. A small increase in the V_{oc} of about 13 mV was observed upon removing the buffer layer. This indicates that the change in doping concentration at the interface layer has a quantifiable but limited impact on V_{oc}, suggesting that other factors, such as the quality of the interface and/or recombination rates may affect the V_{oc} more significantly. Table 4.2 compares the E_a values from the T = 0 K intercept from Fig. 4.9 with and without the SnO_2 buffer layer, with a maximum increase of 24.22 meV for $S_f = 10^5$ cm/s without the buffer layer. The increase in activation energy (E_a) with the removal of the buffer layer suggests small changes in the magnitude of recombination, but not the mechanism (i.e., front surface vs. bulk).

Thus far, studies have assumed a back surface recombination velocity of S_b = 10^5 cm/s. A

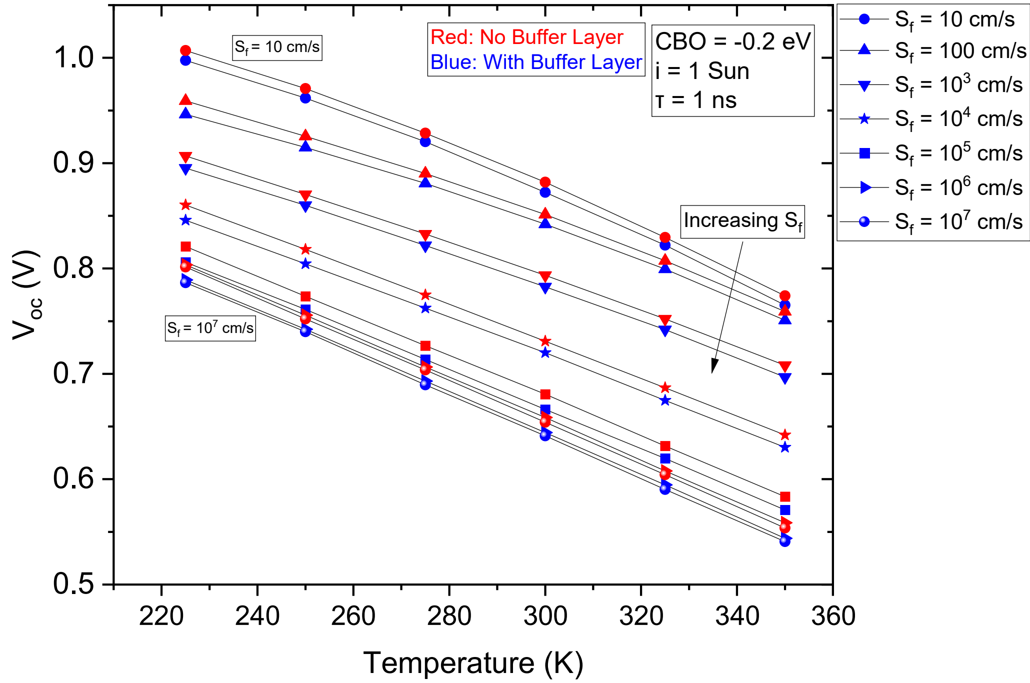

Figure 4.9 V_{oc} vs. T: with SnO_2 (blue line) and the without SnO_2 (red line) buffer layer. The E_a increases by $\approx$ 13 meV for each order of magnitude of S_f.

S_f (cm/s)	E_a: With Buffer Layer (eV)	E_a: Without Buffer Layer (eV)	ΔE_a (meV)
10	1.516	1.530	14
100	1.391	1.405	14
10^3	1.298	1.307	08
10^4	1.258	1.265	07
10^5	1.240	1.264	24
10^6	1.246	1.257	11
10^7	1.244	1.257	13

Table 4.2 Comparison of E_a values with and without the SnO_2 buffer layer. Note: The ΔE_a column is in units of meV. The linear regression fitting error in E_a is about 10 meV.

study focusing on varying the back surface recombination velocity (S_b) was carried out for 1 Sun intensity with parameters of S_f = 1000 cm/s, τ = 5 ns, CBO = -0.2 eV, Φ_{bp} = 0.4 eV, and swept S_b through 10 and 10^7 cm/s. To compare the V_{oc} for the case with and without the SnO_2 buffer layer, JV curves were generated for both cases. Fig. 4.10 is the JV curve in the case without the buffer

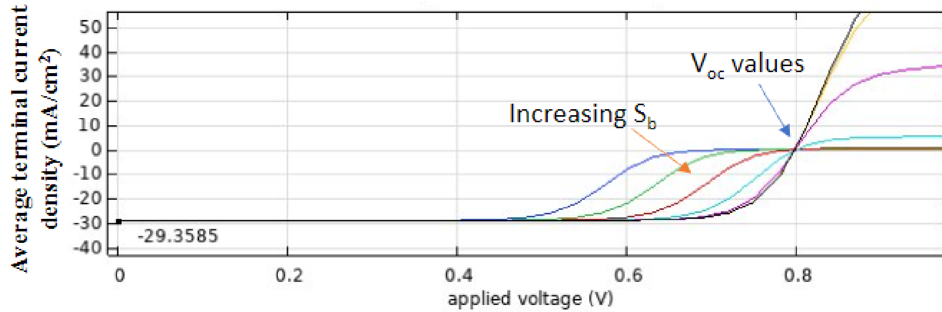

Figure 4.10 Room temperature JV curve without buffer layer at S_f = 100 cm/s, τ = 5 ns, CBO = -0.2 eV, and Φ_{bp} = 0.4 eV: Yields a higher V_{oc} on average of $\approx$ 11.58 mV for S_b = 10 to 10^7 cm/s.

layer, with increasing S_b values, and J_{sc} = -29.36 mA/cm^2. Table 4.3 compares the V_{oc} for the case with and without the buffer layer for a range of back surface recombination velocities, S_b. The V_{oc} was found to increase by $\approx$ 11 - 12 mV over seven orders of magnitude for the S_b. Although S_b has a negligible impact on V_{oc} for the case of Fig. 4.10, it has a significant effect on the forward current and FF. With the large Schottky barrier of 0.4 eV, recombination at the back contact is required to allow forward current to flow. At higher S_b, the current saturates for $V > V_{oc}$ due to the barrier, and that effect is conventionally called JV rollover.

S_b (cm/s)	With Buffer V_{oc} (V)	Without Buffer V_{oc} (V)	ΔV_{oc} (mV)
10	0.789	0.802	12
100	0.790	0.802	12
10^3	0.790	0.802	12
10^4	0.790	0.801	12
10^5	0.787	0.799	11
10^6	0.787	0.798	11
10^7	0.786	0.797	11

Table 4.3 Comparison of V_{oc} values for Se-graded device model with and without the SnO_2 buffer layer for a range of back surface recombination (S_b) values. V_{oc} does not depend on S_b.

The findings imply that while the removal of the buffer layer increases the V_{oc} and E_a by about 10 - 20 mV (or meV), it has only a small effect on the overall device performance. However, careful optimization of the TCO layer, including its doping concentration and interface properties can be crucial for maintaining high device performance.

4.2.1 Back Contact Study

Simulations for the back surface recombination study were run, as detailed in Section 3.2.1 and Table 3.5, and data was extracted for analysis. For CBO = 0 eV (at the Cd(Se,Te)/SnO_2 interface), i = 1 Sun, τ = 1000 ns, and S_f = 100 cm/s, the back surface recombination velocity and back contact barrier height Φ_{bp} were varied to study the effects on the activation energy. To study the low and high back-barrier potential, Φ_{bp} values of 0.2 and 0.4 eV were simulated, along with S_b = 10^5 - 10^7 cm/s.

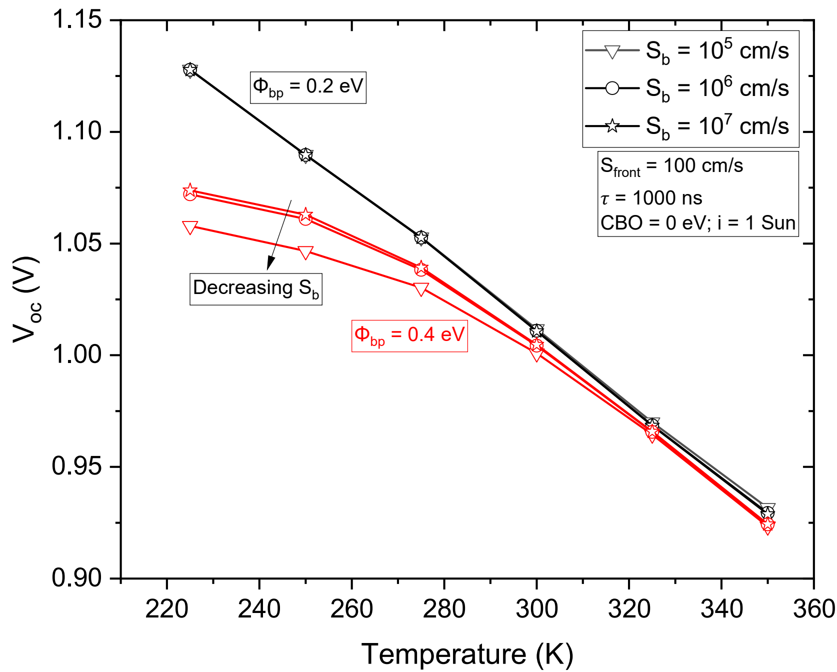

Figure 4.11 Back contact study: V_{oc} vs. T for $\Phi_{bp} = 0.2$ and 0.4 eV. Parameters: CBO = 0 eV, i = 1 Sun, τ = 1000 ns, S_f = 100 cm/s. The V_{oc} is insensitive to S_b at Φ_{bp} = 0.2 eV and yielded $E_a \approx$ 1.5 eV. At Φ_{bp} = 0.4 eV, the E_a reduced to $\approx$ 1.47 eV, and V_{oc} varied with S_b at lower temperatures.

Fig. 4.11 is the V_{oc} vs. temperature plot for the aforementioned parameters. The black lines represent the lower back barrier potential Φ_{bp} = 0.2 eV. The plot shows that the V_{oc} is insensitive to the S_b ranging from 10^5 to 10^7 cm/s, and has $E_a \approx$ 1.50 eV. The red lines in the plot represent the higher back barrier potential Φ_{bp} = 0.4 eV. It shows that in the low-temperature limit

of $T < 300$ K, the V_{oc} line "falls" with a curvature as the temperature decreases. When Φ_{bp} is large, varying S_b significantly reduces the E_a at lower temperatures. The linear fit for the straight-line portion (300 K< $T < 350$ K) of the V_{oc} vs. T plot for Φ_{bp} = 0.4 eV yields $E_a \approx$ 1.47 eV. This curvature may be due to temperature dependencies on parameters such as the effective density of states in the conduction and valence band, thermal velocity, and carrier mobility.

4.2.2 Incorporation of ZnTe:Cu as Back Contact Interface

Back contacts play an essential role in charge collection and the overall efficiency of the device. A Cu-doped ZnTe interface (ZnTe:Cu) of 500 nm thickness and E_g = 2.30 eV was employed between the Cd(Se,Te) absorber layer and back metal contact. The simulations were run as described in Section 3.2.1 and Table 3.6. For CBO = 0 eV (at the Cd(Se,Te)/SnO_2 interface), i = 1 Sun, τ = 1000 ns, S_f = 100 cm/s, Fig. 4.12 shows the V_{oc} vs. T plots for valence band offset (VBO) = 0 eV and -0.4 eV. This VBO is at the Cd(Se,Te)/ZnTe:Cu interface. For no

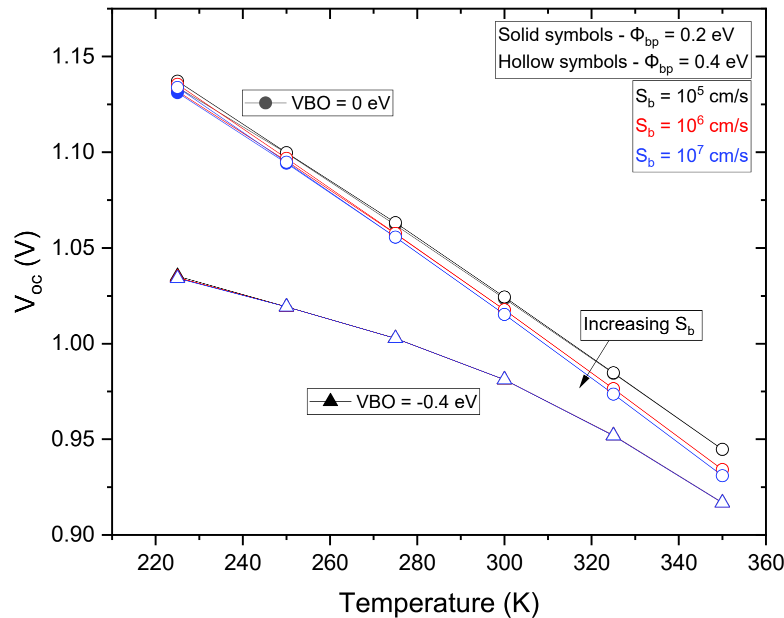

Figure 4.12 V_{oc} vs. T for VBO = 0 eV and -0.4 eV with added ZnTe:Cu interface. Parameters: CBO = 0 eV, i = 1 Sun, τ = 1000 ns, S_f = 100 cm/s. Values of back surface recombination velocity, S_b, and back contact barrier height, Φ_{bp}, are shown in the legend.

valence band offset (VBO = 0 eV shown by circular symbols), the V_{oc} and hence E_a is not significantly affected by the selected ranges of Φ_{bp} and S_b. $E_a \approx$ 1.51 eV for VBO = 0 eV. For VBO = -0.4 eV (triangle symbols in the plot), the activation energy is uncertain because there appears to be no linear region in the $V_{oc}(T)$. The reason for that temperature dependence is unclear at the present time.

To examine how E_a changes with the VBO, a E_a vs. VBO plot was made for CBO = 0 eV (at Cd(Se,Te)/SnO_2 interface), i = 1 Sun, τ = 1000 ns, S_f = 100 cm/s, over Φ_{bp} = 0.2, 0.4 eV and S_b = 10^5 - 10^7 cm/s (shown by various symbols in the legend). The red lines represent Φ_{bp} = 0.4 eV while the black lines represent Φ_{bp} = 0.2 eV. Fig. 4.13 shows that the activation energy decreases almost linearly as the VBO becomes more positive. It was also observed that varying the Φ_{bp} and S_b had smaller effects on the E_a values. For VBO = -0.2, 0, 0.2, and 0.4 eV, the E_a varied in the range of 1.46 - 1.52 eV.

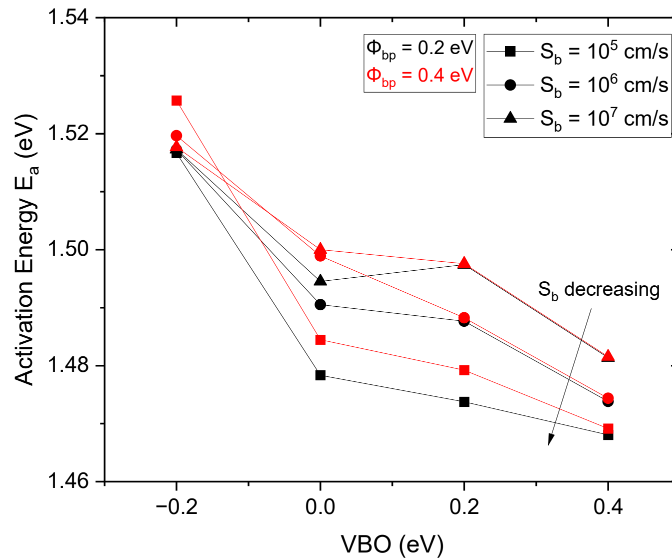

Figure 4.13 E_a with changing VBO at various back surface recombination velocities, S_b, and back contact barriers, Φ_{bp}. The E_a ranges from $\approx$ 1.46 - 1.52 eV across the VBO values.

4.3 Uniterns: Uniform Se Device Without Buffer Layer

All the previous devices discussed have had a selenium grading throughout (See Fig. 3.7). This section will focus on the results of simulating a device with constant Se in the absorber layer. After running the simulations described in Section 3.2.1 and Table 3.7, the data was extracted and

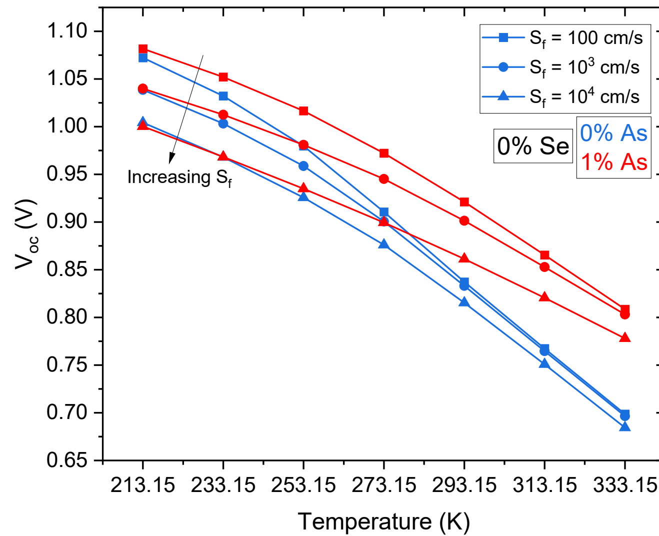

Figure 4.14 V_{oc} vs. T plots for Uniterns - 0% Se. Parameters: CBO = -0.2 eV, S_b = 10^5 cm/s, i = 1 Sun. Curvature in $V_{oc}(T)$ that may be explained by temperature dependence of parameters such as mobility (μ(T)), thermal velocity ($v_{th}(T)$), and effective density of states in the conduction band ($N_C(T)$) and valence band ($N_V(T)$).

analyzed. Fig. 4.14 is the V_{oc} vs. T plot for 0% Se, with two As doping concentrations - 0% As (blue plot) and 1% As (red plot) for S_f = 100 to 10^4 cm/s. As mentioned in Section 3.2.1, 0% and 1% As correspond to p-type doping of 10^{14} and 10^{15} cm^{-3}, respectively, in the device models with 0% Se, that is, pure CdTe, with a band gap of 1.5 eV. At higher temperatures ($T > 275$ K), there seems to be a significant difference between the V_{oc} for the two As dopings. The 1% As doping yields a higher V_{oc}, but as the temperature decreases ($T < 273$ K), the difference between the V_{oc} starts decreasing for the two As doping levels. The curvature observed in the $V_{oc}(T)$ plot is likely influenced by the temperature dependence of various parameters, including mobility (μ(T)), thermal velocity ($v_{th}(T)$), and effective density of states both in the conduction band

($N_C(T)$) and valence band ($N_V(T)$) as discussed in Section 2.5. This non-linearity is more evident when Se doping is lower.

In the case of 20% and 40% Se concentration, the V_{oc} vs. T plots are given in Fig. 4.15. The solid symbols represent 20% Se while the hollow symbols represent 40% Se. It was observed that the V_{oc} declines upon increasing the Se concentration. S_f = 100 cm/s yielded the maximum V_{oc} difference between 20% and 40% Se, while S_f = 10^4 cm/s yielded the lowest V_{oc} difference. The 20% Se device had doping of 2×10^{16} cm^{-3} and a uniform band gap of 1.41 eV (based on Se-content), while the 40% Se device had doping of 8×10^{15} cm^{-3} and a band gap of 1.36 eV. The lowered band gap and doping of the 40% Se should result in lower V_{oc}, as observed in Fig. 4.15.

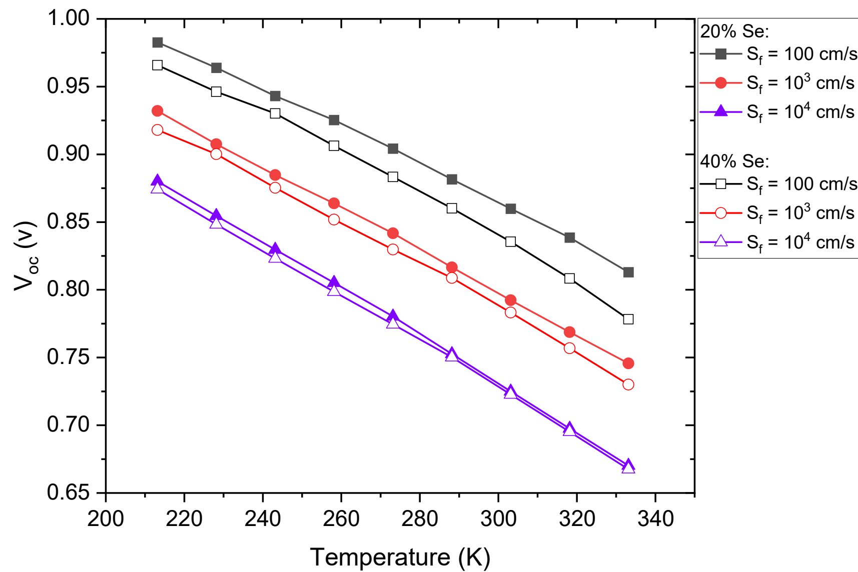

Figure 4.15 V_{oc} vs. T plots for Uniterns - 20% Se and 40% Se. Parameters: CBO = -0.2 eV, S_b = 10^5 cm/s, i = 1 Sun.

4.4 Comparing Simulations with Experimental Data

JVTi data provided by NREL for device V617 is shown in Fig. 4.16. Device details and performance metrics are provided in Section 3.1, with V_{oc} = 0.75 V. The goal is to improve performance to $V_{oc} \geq$ 0.90 V. In the high-temperature region ($T >$ 290 K), the y-intercept E_a =

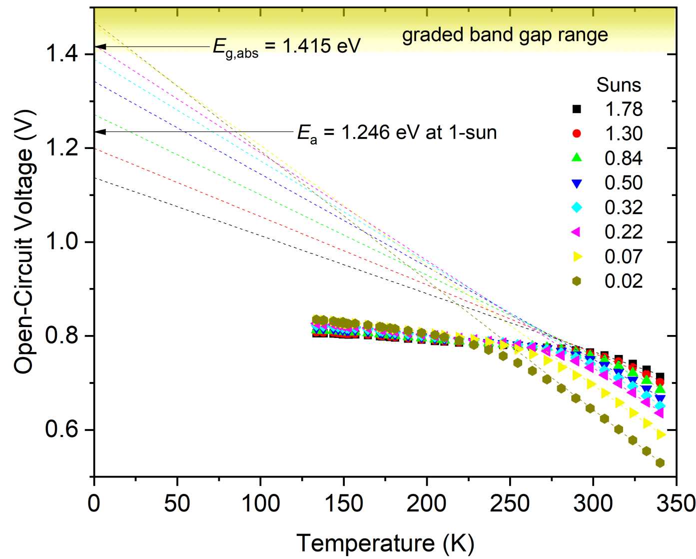

Figure 4.16 $V_{oc}(T)$ for a range for light intensities i = 0.02 - 1.78 Suns. Linear fits of the high-temperature region provide the E_a. The absorption band gap, $E_{g,abs}$, from the QE inflection point is shown.

1.470 $\pm$ 0.014 eV at 0.02 Sun decreases to E_a = 1.137 $\pm$ 0.033 eV at 1.78 Sun. Focusing near operating conditions, the higher temperature linear regime interpolated to 1 Sun gives E_a = 1.246 $\pm$ 0.036 eV, which is below the graded bandgap range (E_g = 1.4 - 1.5 eV) at room temperature. Accounting for band gap temperature dependence yields E_a = 1.216 eV at T = 300 K (band tails are neglected). That suggests a cliff-like conduction band offset, CBO = ΔE_c = E_a - $E_g \approx$ -0.2 eV, at the front interface (assuming E_g = 1.415 eV).

For CBO = -0.2 eV simulations were compared to V_{oc} (T) data to find the optimal range of S_f and τ [29]. Fig. 4.17 shows the V_{oc} vs. T plot over a range of S_f and τ at 1 sun intensity. The simulations (shaded regions) and data (points) are similar for $S_f \approx 10^3$ - 10^4 cm/s. While bulk lifetimes are uncertain, it is within the parameter space of τ = 1 - 1000 ns. This means that under these conditions, the front surface recombination dominates V_{oc} loss, even at the lowest bulk

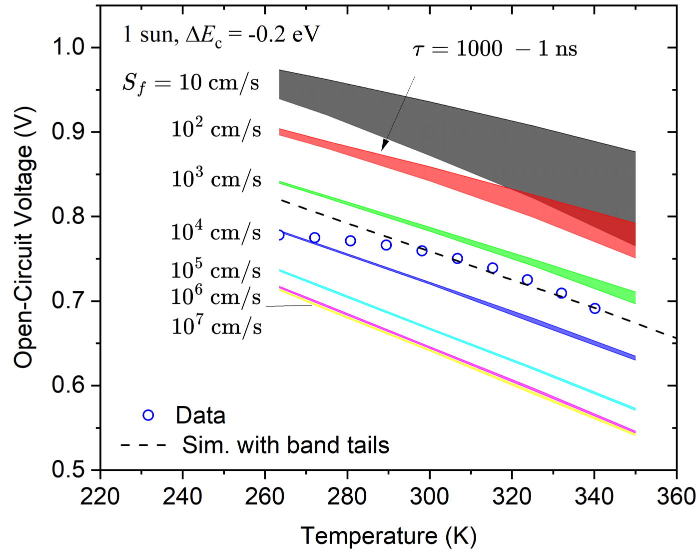

Figure 4.17 V_{oc} (T) at i = 1 Sun and CBO = ΔE_c = -0.2 eV. Each shaded region (simulation) is for a specified S_f within a range of τ= 1 - 1000 ns. Data (points) are between S_f = 10^3 - 10^4 cm/s. Band tails are included in the simulation (dashed line).

lifetime τ = 1 ns. It can also be observed that as S_f increases, the V_{oc} becomes less sensitive to τ. Note that the simulations do not account for certain temperature dependencies, especially for $T <$ 300 K. These dependencies are described in Section 2.5. Based on the simulation analysis for this device, it was determined that front-surface recombination dominates V_{oc} losses with CBO = -0.2 eV and S_f = 1000 cm/s. Minimizing front surface recombination and band offset is crucial for improving V_{oc} for device V617.

CHAPTER 5 CONCLUSIONS

This thesis aims to investigate the impact of the bulk as well as front and back surface recombination on the open circuit voltage, V_{oc}, of thin-film photovoltaic devices. Various Cd(Se,Te) device models were studied throughout this computational research, and simulations of JVTi were carried out using COMSOL Multiphysics software. The research findings are detailed below.

- JVTi simulations and measurements can quantify V_{oc} losses due to front surface recombination and provide insight to heterojunction band alignment in certain important cases. In particular, that is true when there is a "cliff"-like conduction band alignment and recombination active defects at the front surface.
- The bandgap grading that is typical for modern Cd(Se,Te) devices results in a smaller band gap at the front interface. That can exacerbate interface recombination due to lower activation energy, E_a. Basically, front interface defects become more critical when the interface band gap is smaller.
- If the E_a from JVTi equals the bulk band gap, then V_{oc} recombination losses may occur at the front interface or within the bulk.
- At a CBO = -0.2 eV, E_a increases significantly with the light intensity when $S_f < 10^4$ cm/s and $\tau < 100$ ns, and indicates a possible shift from front interface (low E_a) to bulk (higher E_a) recombination as light intensity decreases.
- Replacing the SnO_2 buffer layer with the TCO layer increases the V_{oc} and E_a by $\approx$ 10 - 20 meV, causing only a small impact on device performance.
- While studying the back surface recombination, it was found that when the back barrier potential to holes Φ_{bp} is larger (0.4 eV in this case), varying the S_b significantly reduces the activation energy at lower temperatures. The curvature of $V_{oc}(T)$ is not understood presently.

- Upon incorporating ZnTe:Cu as a back contact interface, it was found that a VBO = -0.2 eV yielded the highest E_a value $\approx$ 1.52 eV for CBO = 0 eV (at Cd(Se,Te)/SnO_2 interface), i = 1 Sun, τ = 1000 ns, S_f = 100 cm/s.

- Back surface recombination was found to have minimal impact on V_{oc} for the Cd(Se,Te) device parameters studied herein.

- Curvatures observed in some $V_{oc}(T)$ plots are likely influenced by the temperature dependence of various parameters, including mobility (μ(T)), thermal velocity ($v_{th}(T)$), and effective density of states both in the conduction band ($N_C(T)$) and valence band ($N_V(T)$). This non-linearity is more evident at lower Se doping levels.

- Comparing simulations to JVTi data provided by NREL indicates that front surface recombination dominates V_{oc} losses in that device. It was estimated that for S_f = 10^3 cm/s and CBO = -0.2 eV, adjusting the band alignment to CBO = 0 eV and reducing S_f would significantly increase V_{oc}.

CHAPTER 6 FUTURE WORK

In this section, the research and scope highlighted in *"CdTe-based thin film photovoltaics: Recent advances, current challenges, and future prospects"* [8] is delineated. A primary goal to improve the V_{oc} by maximizing photocarrier lifetime is by mitigating non-radiative recombination within the bulk and at the front buffer/absorption interface while addressing bandgap disorder [35]. Provided that the photocarrier lifetimes are far below the radiative limit, and assuming that at this limit V_{oc} remains independent of absorber doping, V_{oc} improvements may also be achieved by increasing doping levels. However, increased doping can lead to voltage fluctuations due to poor dopant activation, often manifesting as sub-bandgap absorption and hence constraining voltage [37].

Further improvements in V_{oc} will stem from optimizing front and back contacts to achieve carrier-selective, low-resistance, energy-level-matched Ohmic contacts. The term "Ohmic" denotes no energy level offset from absorber to contact, ensuring thermodynamic reversibility without voltage losses. These properties will enable photocarriers to be extracted at V_{oc}, equivalent to the internal quasi-Fermi level splitting that quantifies stored electrical potential energy in the form of excess carrier concentrations, and hence at the respective quasi-Fermi levels without losing photocurrent (J_{sc}) or incurring voltage losses from energy level offsets or resistance losses through the contact layers. It is highlighted that the next generations of CdTe-based cell technology match high-efficiency cells, where carrier-selective contacts extract carriers and voltage via diffusive transport from an absorber with a bulk lifetime nearing the radiative limit.

Within the scope of this thesis, JVTi simulation should be employed to analyze data from a broad range of higher efficiency devices to determine the limitations of JVTi for distinguishing bulk, front surface, and back surface recombination.

BIBLIOGRAPHY

[1] Solar Energy Technologies Office, "SETO Timeline," n.d. Accessed: April 2024.

[2] H. Ritchie, P. Rosado, and M. Roser, "Energy production and consumption," *Our World in Data*, 2020. https://ourworldindata.org/energy-production-consumption.

[3] Connor O'Neil and Harrison Dreves, "Building a solar-powered future," 2022. Accessed: April 2024.

[4] David Feldman et al, "Fy2023 annual progress report," 2023. Accessed: April 2024.

[5] U.S. Department of Energy, "Solar photovoltaic cell basics," Accessed: 2024.

[6] W. Shockley and H. J. Queisser, "Detailed Balance Limit of Efficiency of *p-n* Junction Solar Cells," *Journal of Applied Physics*, vol. 32, pp. 510–519, Mar. 1961.

[7] National Renewable Energy Laboratory, "Solar photovoltaic cell efficiency," Accessed: 2024.

[8] M. A. Scarpulla, B. McCandless, A. B. Phillips, Y. Yan, M. J. Heben, C. Wolden, G. Xiong, W. K. Metzger, D. Mao, D. Krasikov, I. Sankin, S. Grover, A. Munshi, W. Sampath, J. R. Sites, A. Bothwell, D. Albin, M. O. Reese, A. Romeo, M. Nardone, R. Klie, J. M. Walls, T. Fiducia, A. Abbas, and S. M. Hayes, "CdTe-based thin film photovoltaics: Recent advances, current challenges and future prospects," *Solar Energy Materials and Solar Cells*, vol. 255, p. 112289, June 2023.

[9] A. H. Munshi, J. Kephart, A. Abbas, J. Raguse, J.-N. Beaudry, K. Barth, J. Sites, J. Walls, and W. Sampath, "Polycrystalline CdSeTe/CdTe Absorber Cells With 28 mA/cm ^{2} Short-Circuit Current," *IEEE Journal of Photovoltaics*, vol. 8, pp. 310–314, Jan. 2018.

[10] A. H. Munshi, J. M. Kephart, A. Abbas, T. M. Shimpi, K. L. Barth, J. M. Walls, and W. S. Sampath, "Polycrystalline CdTe photovoltaics with efficiency over 18% through improved

absorber passivation and current collection," *Solar Energy Materials and Solar Cells*, vol. 176, pp. 9–18, Mar. 2018.

[11] R. E. Brandt, N. M. Mangan, J. V. Li, Y. S. Lee, and T. Buonassisi, "Determining interface properties limiting open-circuit voltage in heterojunction solar cells," *Journal of Applied Physics*, vol. 121, p. 185301, May 2017.

[12] S. Rühle, "Tabulated values of the Shockley–Queisser limit for single junction solar cells," *Solar Energy*, vol. 130, pp. 139–147, June 2016.

[13] J. M. Burst, J. N. Duenow, D. S. Albin, E. Colegrove, M. O. Reese, J. A. Aguiar, C.-S. Jiang, M. Patel, M. M. Al-Jassim, D. Kuciauskas, S. Swain, T. Ablekim, K. G. Lynn, and W. K. Metzger, "CdTe solar cells with open-circuit voltage breaking the 1 V barrier," *Nature Energy*, vol. 1, p. 16015, Feb. 2016.

[14] D. Krasikov, D. Guo, S. Demtsu, and I. Sankin, "Comparative study of As and Cu doping stability in CdSeTe absorbers," *Solar Energy Materials and Solar Cells*, vol. 224, p. 111012, June 2021.

[15] W. K. Metzger, D. W. Miller, R. Mallick, X. Li, W. Zhang, I. Wang, A. Polizzotti, T. Ablekim, D. H. Cao, D. C. Hamilton, J. Bailey, C. Lee, S. Grover, D. Lu, and G. Xiong, "As-Doped CdSeTe Solar Cells Achieving 22% Efficiency With 0.23%/°C Temperature Coefficient," *IEEE Journal of Photovoltaics*, vol. 12, pp. 1435–1438, Nov. 2022.

[16] E. Colegrove, B. Good, A. Abbas, H. Moutinho, S. Johnston, C.-S. Jiang, P. O'Keefe, J. M. Walls, D. S. Albin, and M. O. Reese, "Investigating the role of copper in arsenic doped Cd(Se,Te) photovoltaics," *Solar Energy Materials and Solar Cells*, vol. 246, p. 111886, Oct. 2022.

[17] P. Gorai, D. Krasikov, S. Grover, G. Xiong, W. K. Metzger, and V. Stevanovic, "A Search for New Back Contacts for CdTe Solar Cells,"

[18] S. Kret, P. Dłużewski, P. Dłużewski, and J.-Y. Laval, "On the measurement of dislocation core distributions in a gaas/znte/cdte heterostructure by high-resolution transmission electron microscopy," *Philosophical Magazine*, vol. 83, no. 2, pp. 231–244, 2003.

[19] J. V. Li, S. Grover, M. A. Contreras, K. Ramanathan, D. Kuciauskas, and R. Noufi, "A recombination analysis of Cu(In,Ga)Se2 solar cells with low and high Ga compositions," *Solar Energy Materials and Solar Cells*, vol. 124, pp. 143–149, May 2014.

[20] X. Fang, S. Ren, C. Li, C. Li, G. Chen, H. Lai, J. Zhang, and L. Wu, "Investigation of recombination mechanisms of CdTe solar cells with different buffer layers," *Solar Energy Materials and Solar Cells*, vol. 188, pp. 93–98, Dec. 2018.

[21] M. D. Mia, C. H. Swartz, S. Paul, S. Sohal, C. R. Grice, Y. Yan, M. Holtz, and J. V. Li, "Electrical and optical characterization of CdTe solar cells with CdS and CdSe buffers—A comparative study," *Journal of Vacuum Science & Technology B, Nanotechnology and Microelectronics: Materials, Processing, Measurement, and Phenomena*, vol. 36, p. 052904, Sept. 2018.

[22] Delft University of Technology, "Solar energy - section 9.1-9.3," n.d. Accessed: April 2024.

[23] PV Education, "PV Education." https://www.pveducation.org/, n.d. Accessed: April 2024.

[24] Park, "Diode characteristics." https://www.iue.tuwien.ac.at/phd/park/node31.html, 2002. Accessed: April 2024.

[25] PV Manufacturing, "Recombination processes." https://pv-manufacturing.org/metrology/recombination-processes/, n.d. Accessed: April 2024.

[26] J. Fox and L. Sun, *Simulation of Time Resolved Photoluminescence to Distinguish Bulk and Interface Recombination in Cd(Se,Te) Photovoltaic Devices*. Bowling Green State University, 2022.

[27] W. Sark, P. Verlinden, A. Reinders, and A. Freundlich, eds., *Photovoltaic Solar Energy: From Fundamentals to Applications*. Chichester, UK: John Wiley & Sons, Ltd, 2016.

[28] M. Nardone, *Photovoltaic device modeling: a multi-scale, multi-physics approach*, ch. 5, pp. 103–134. No. Vol. 166 in IET Energy Engineering Series, The Institution of Engineering and Technology, 2020.

[29] M. Nardone, S. Gupta, E. Mulloy, S. Johnston, E. Colegrove, J. Duenow, B. Good, D. Kuciauskas, and M. Reese, "Comprehensive model for evaluating voltage losses and performance improvements in thin-film photovoltaic devices," *In Progress*, 2024.

[30] "Band offset — Wikipedia, the free encyclopedia." `https://en.wikipedia.org/wiki/Band_offset`, 2024. [Online; accessed 25-April-2024].

[31] S. A. Al Kuhaimi, N. M. Shaalan, and S. Bahammam, "The electron affinity difference in CdS/CdTe solar cells," *Proceedings / Indian Academy of Sciences*, vol. 110, pp. 199–206, June 1998.

[32] Y. Chen, X. Tan, S. Peng, C. Xin, A. E. Delahoy, K. K. Chin, and C. Zhang, "The Influence of Conduction Band Offset on CdTe Solar Cells," *Journal of Electronic Materials*, vol. 47, pp. 1201–1207, Feb. 2018.

[33] T. K. Al-Hamdi, S. W. McPherson, S. K. Swain, J. Jennings, J. N. Duenow, X. Zheng, D. Albin, T. Ablekim, E. Colegrove, M. Amarasinghe, A. Ferguson, W. K. Metzger, C. Szeles, and K. G. Lynn, "CdTe synthesis and crystal growth using the high-pressure Bridgman technique," *Journal of Crystal Growth*, vol. 534, p. 125466, Mar. 2020.

[34] "COMSOL Multiphysics," 2024. Accessed: April 10, 2024.

[35] A. Kanevce, M. O. Reese, T. M. Barnes, S. A. Jensen, and W. K. Metzger, "The roles of carrier concentration and interface, bulk, and grain-boundary recombination for 25% efficient CdTe solar cells," *Journal of Applied Physics*, vol. 121, p. 214506, June 2017.

[36] D. Suthar, S. Chuhadiya, R. Sharma, Himanshu, and M. S. Dhaka, "An overview on the role of ZnTe as an efficient interface in CdTe thin film solar cells: a review," *Materials Advances*, vol. 3, no. 22, pp. 8081–8107, 2022.

[37] W. K. Metzger, S. Grover, D. Lu, E. Colegrove, J. Moseley, C. L. Perkins, X. Li, R. Mallick, W. Zhang, R. Malik, J. Kephart, C.-S. Jiang, D. Kuciauskas, D. S. Albin, M. M. Al-Jassim, G. Xiong, and M. Gloeckler, "Exceeding 20% efficiency with in situ group V doping in polycrystalline CdTe solar cells," *Nature Energy*, vol. 4, pp. 837–845, Aug. 2019.

APPENDIX A 3D Plots: E_a vs. S_f vs. τ

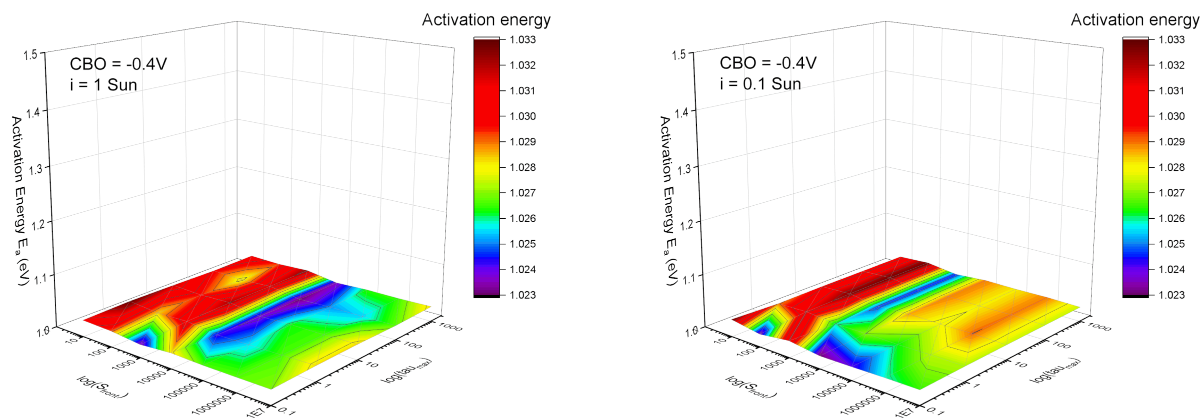

(a) i = 1 Sun (b) i = 0.1 Sun

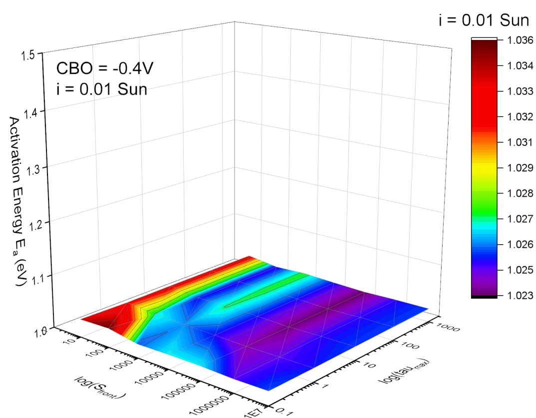

(c) i = 0.01 Sun

Figure 1 E_a vs. S_f vs. τ plots: CBO = -0.4 eV, i = 1, 0.1, 0.01 Suns

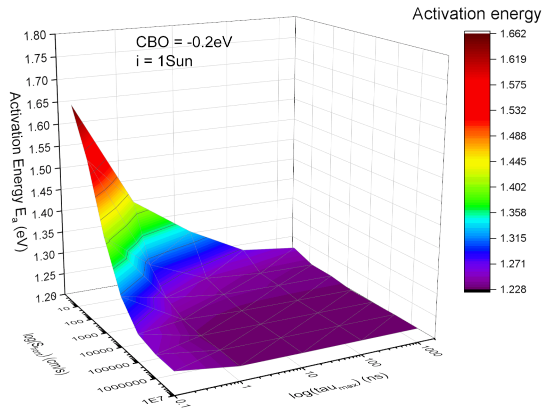

(a) i = 1 Sun

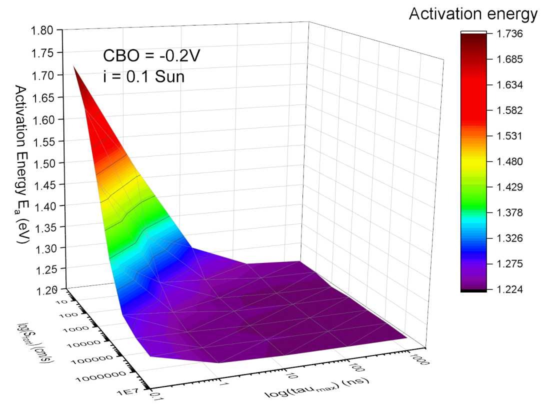

(b) i = 0.1 Sun

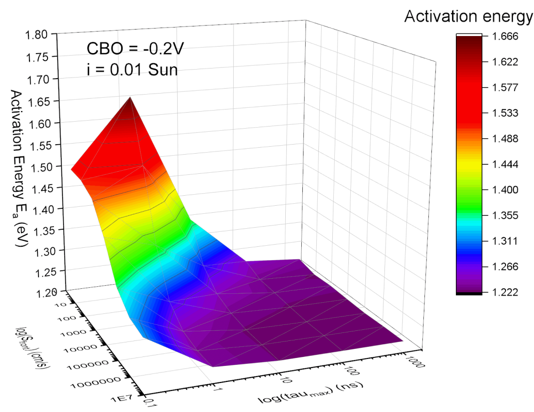

(c) i = 0.01 Sun

Figure 2 E_a vs. S_f vs. τ plots: CBO = -0.2 eV, i = 1, 0.1, 0.01 Suns

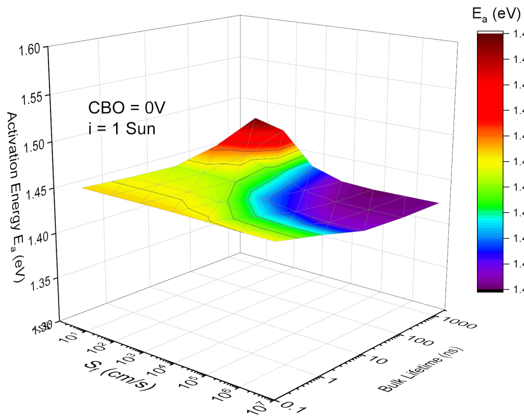

(a) i = 1 Sun

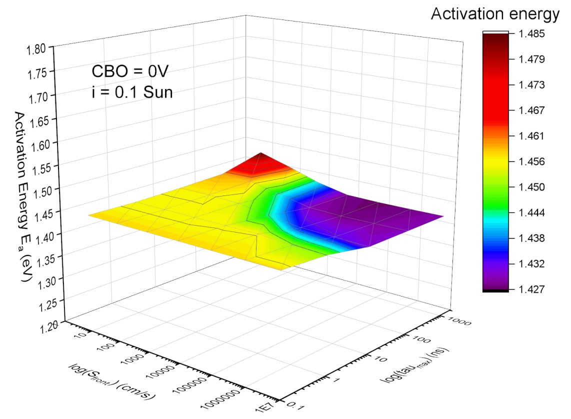

(b) i = 0.1 Sun

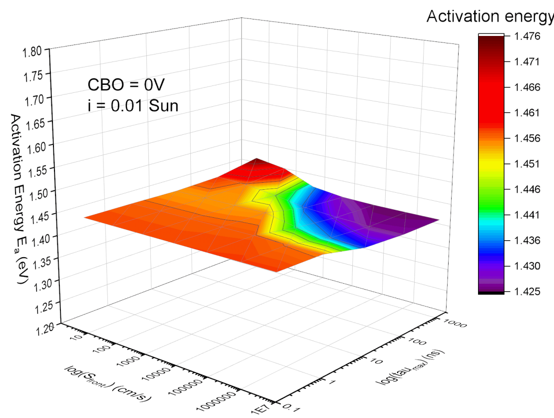

(c) i = 0.01 Sun

Figure 3 E_a vs. S_f vs. τ plots: CBO = 0 eV, i = 1, 0.1, 0.01 Suns

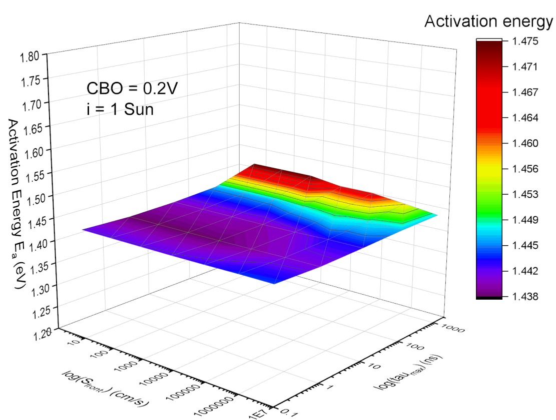

(a) i = 1 Sun

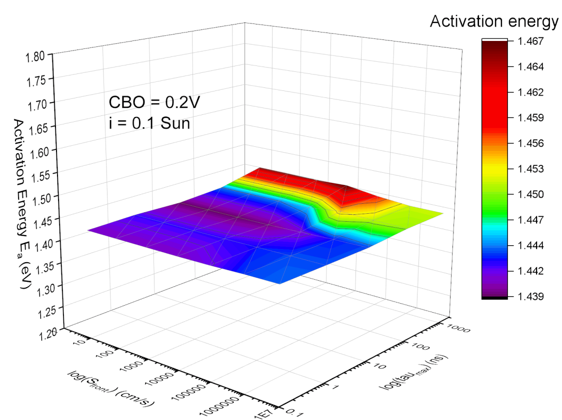

(b) i = 0.1 Sun

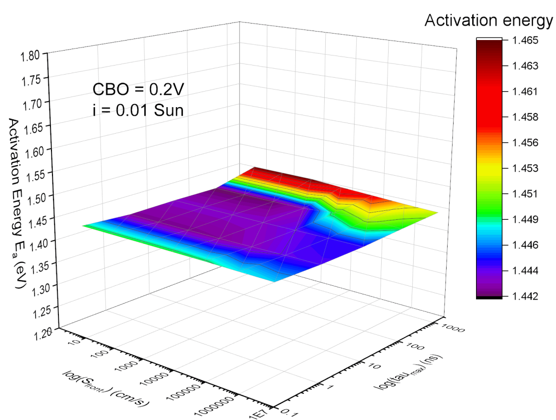

(c) i = 0.01 Sun

Figure 4 E_a vs. S_f vs. τ plots: CBO = 0.2 eV, i = 1, 0.1, 0.01 Suns

APPENDIX B JVTi: V_{oc} vs. T plots

The following pages show V_{oc} vs. T plots generated for this research. Each page of plots is for a particular conduction band offset (CBO) and light intensity (i) value. The plots are for CBO = 0, 0.2, -0.2, -0.4 eV and i = 1, 0.1, 0.01 Sun. Each plot is for a bulk lifetime of τ = 0.1 - 1000 ns. In each plot, every line is for a specific front surface recombination velocity, S_f ranging from 10 - 10^7 cm/s.

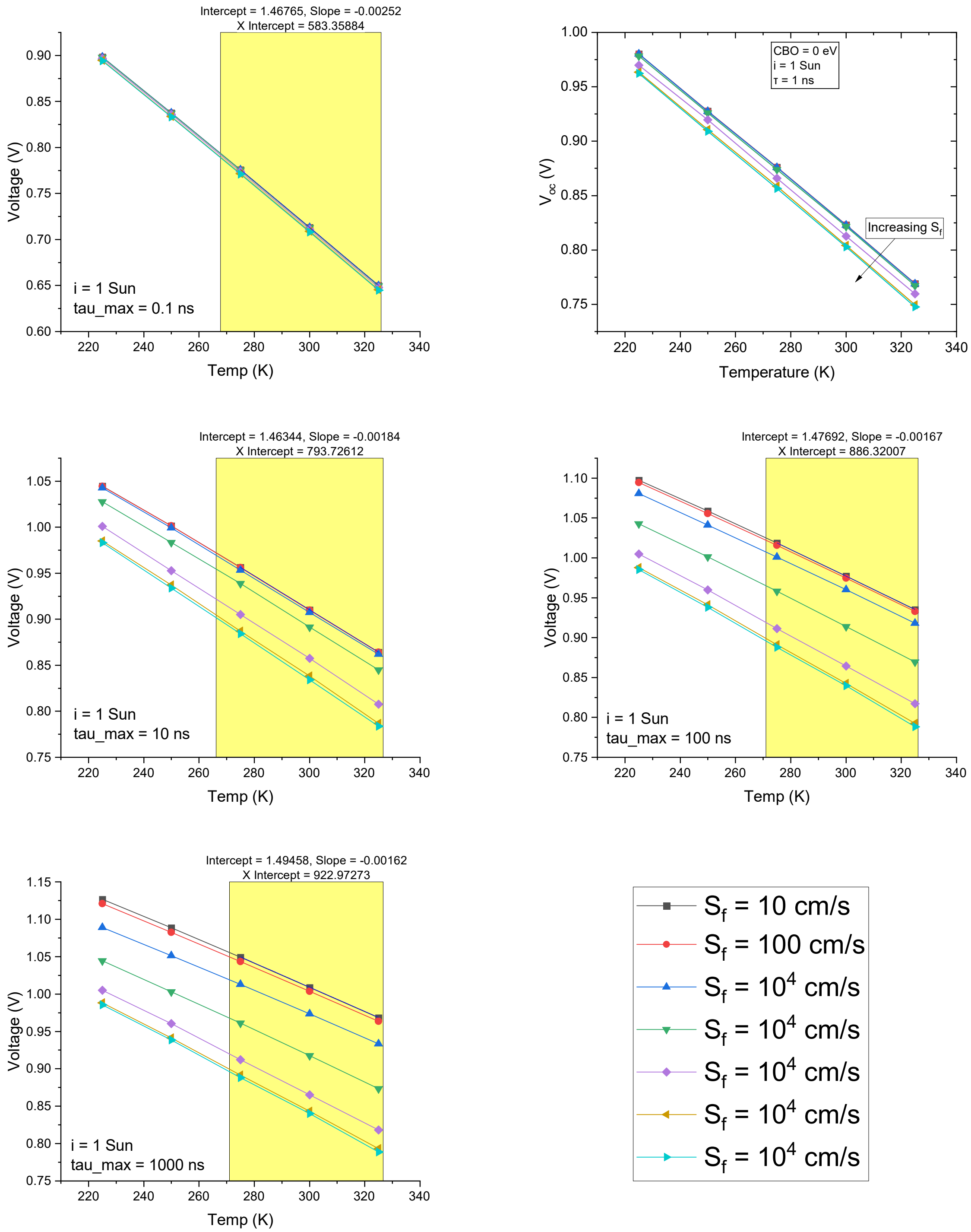

Figure 5 V_{oc} vs. T for CBO = 0 eV, i = 1 Sun

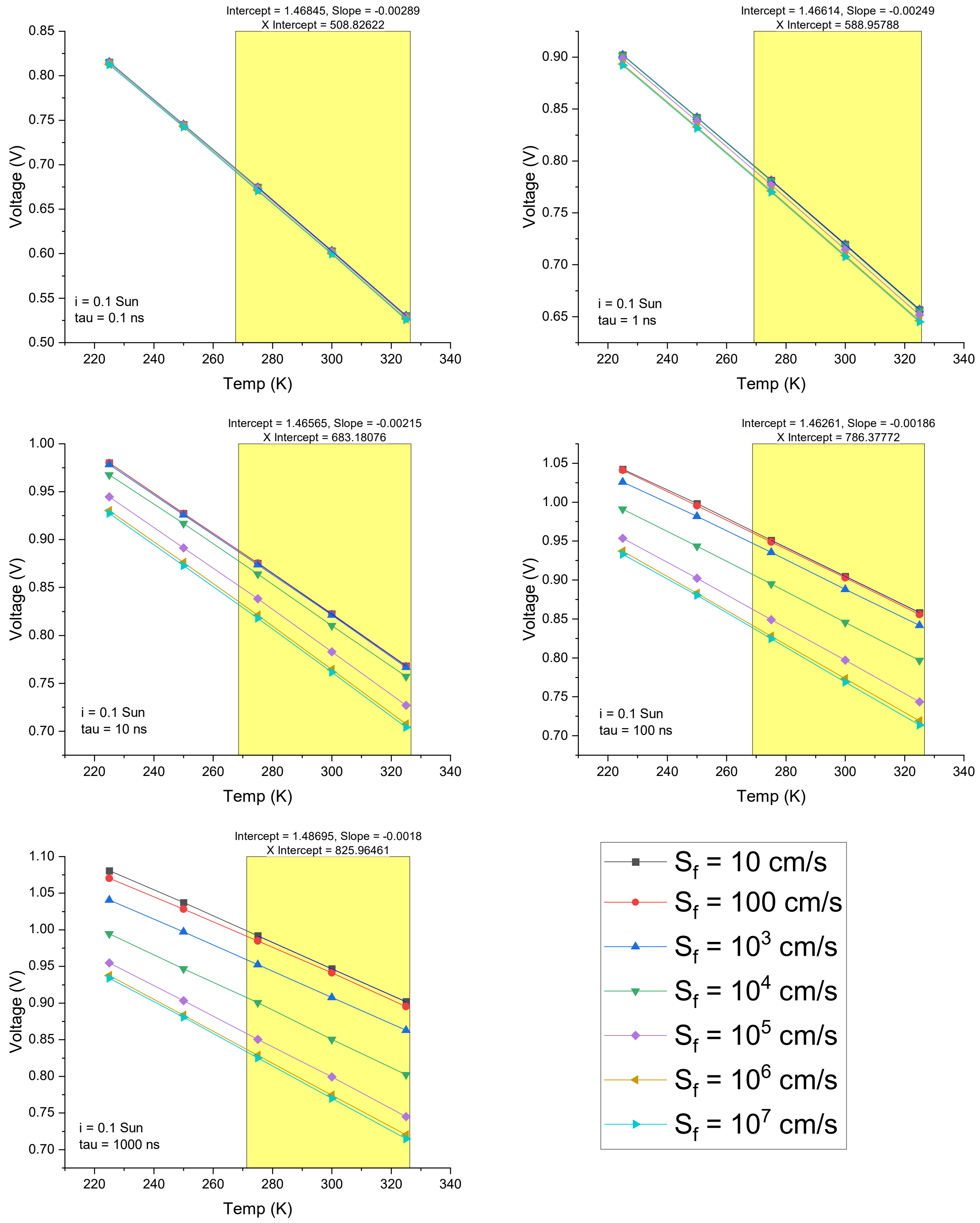

Figure 6 V_{oc} vs. T for CBO = 0 eV, i = 0.1 Sun

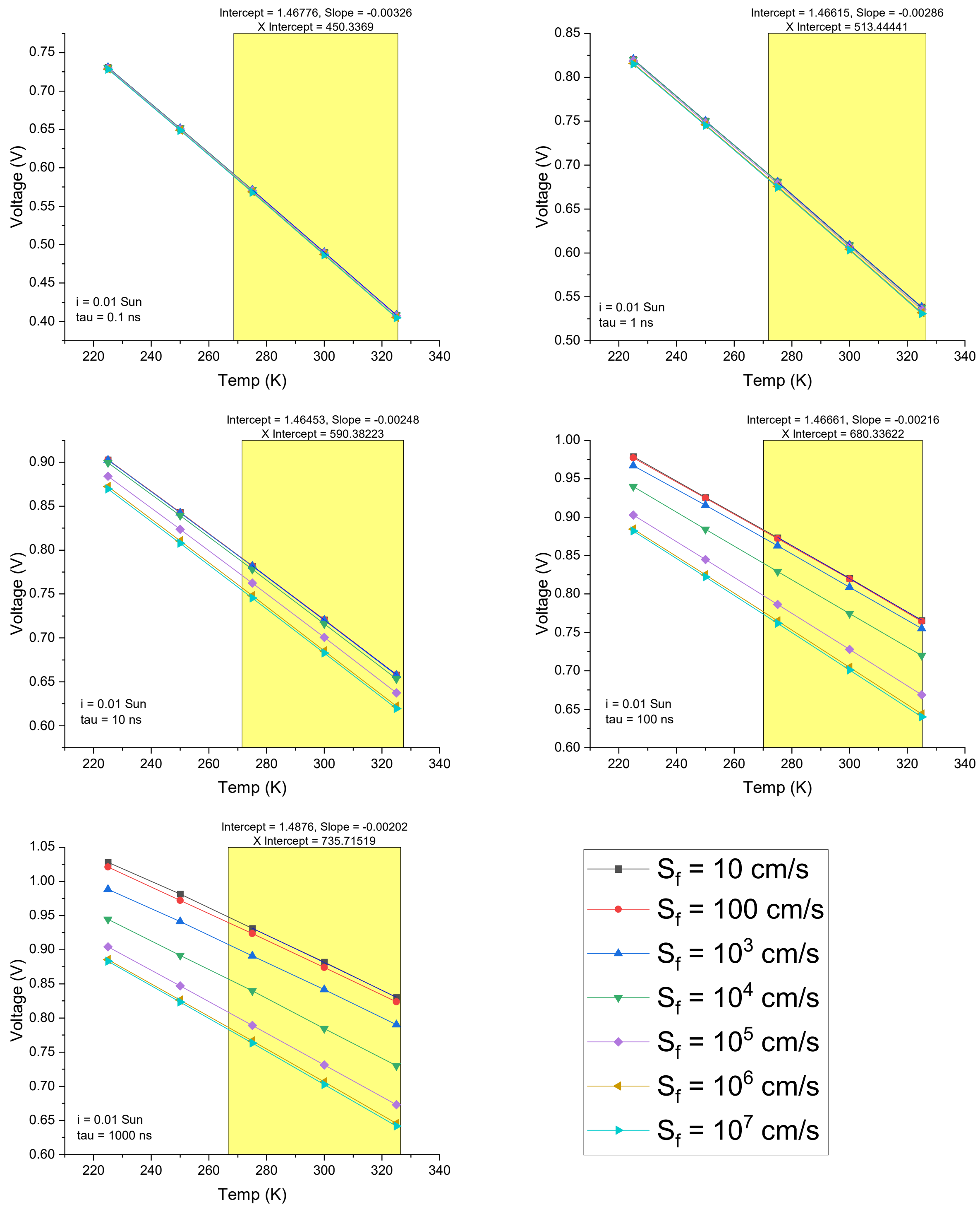

Figure 7 V_{oc} vs. T for CBO = 0 eV, i = 0.01 Sun

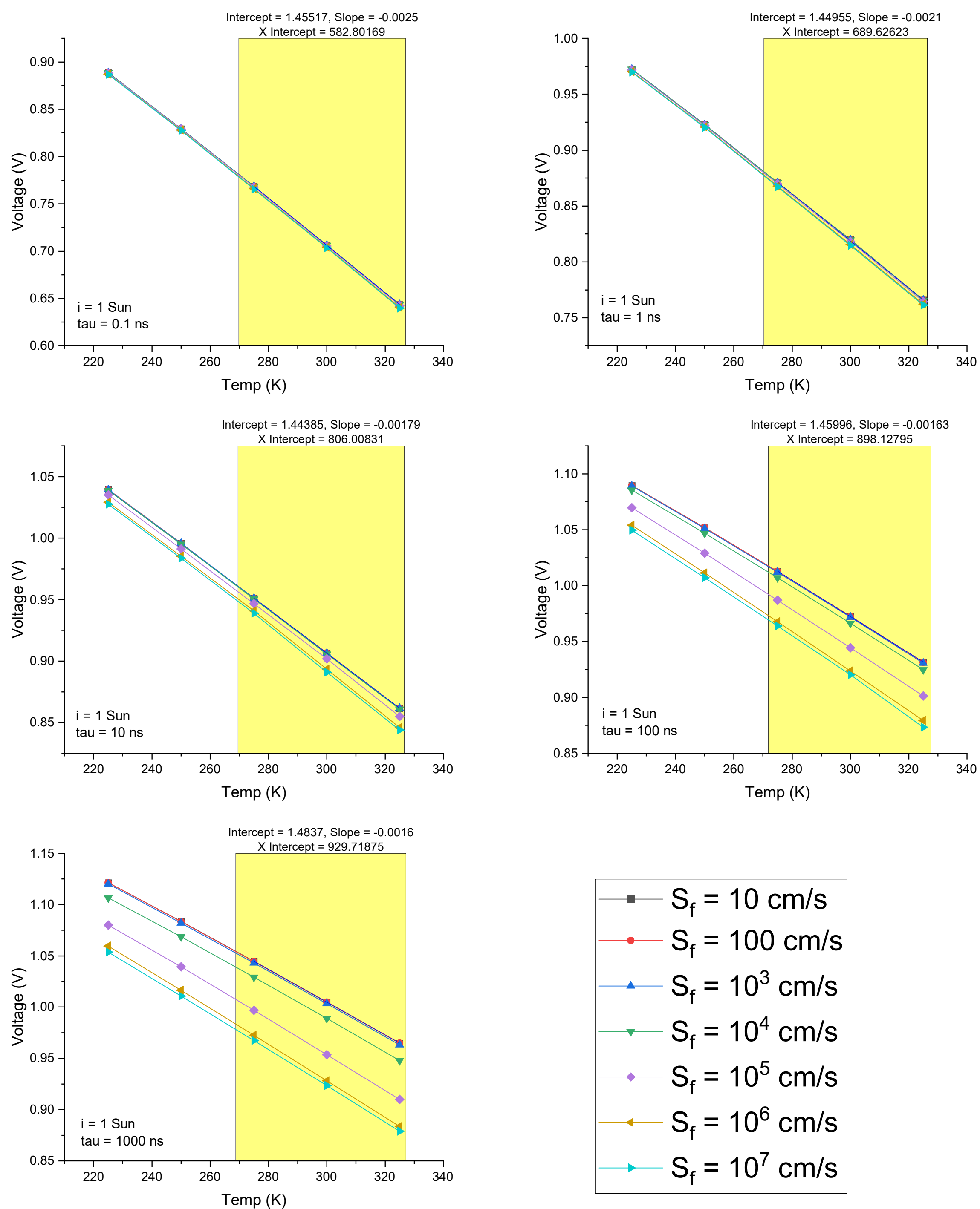

Figure 8 V_{oc} vs. T for CBO = 0.2 eV, i = 1 Sun

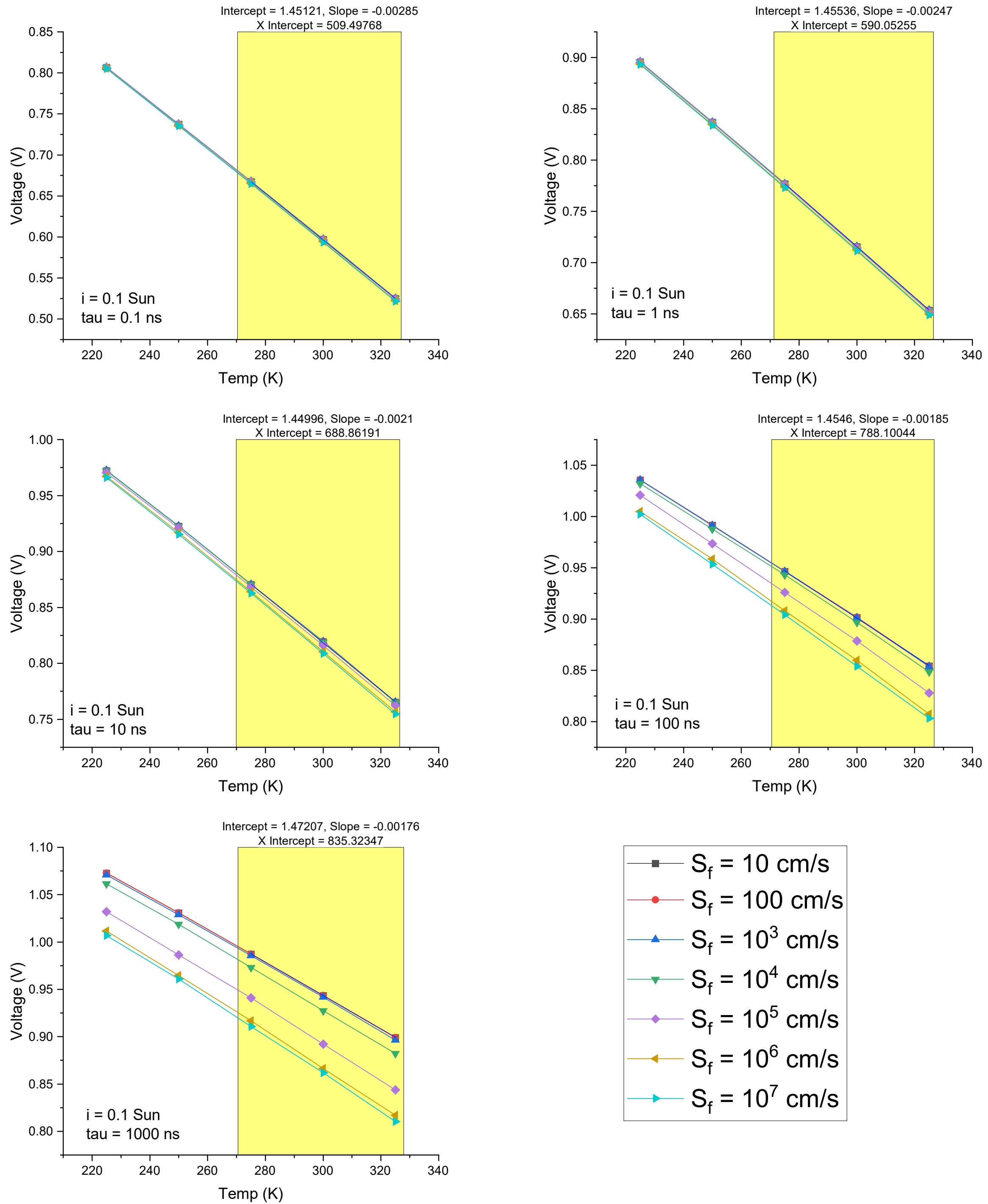

Figure 9 V_{oc} vs. T for CBO = 0.2 eV, i = 0.1 Sun

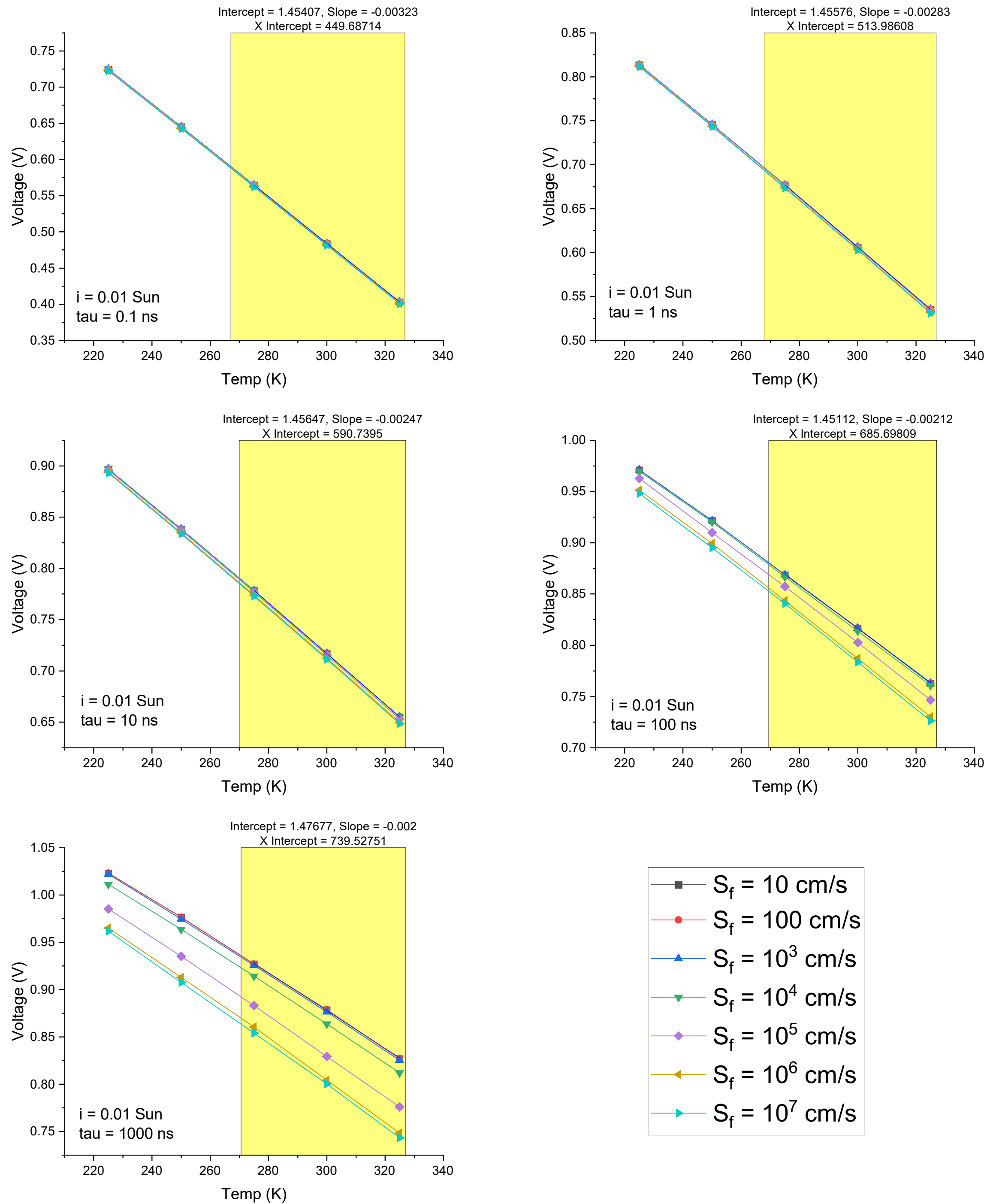

Figure 10 V_{oc} vs. T for CBO = 0.2 eV, i = 0.01 Sun

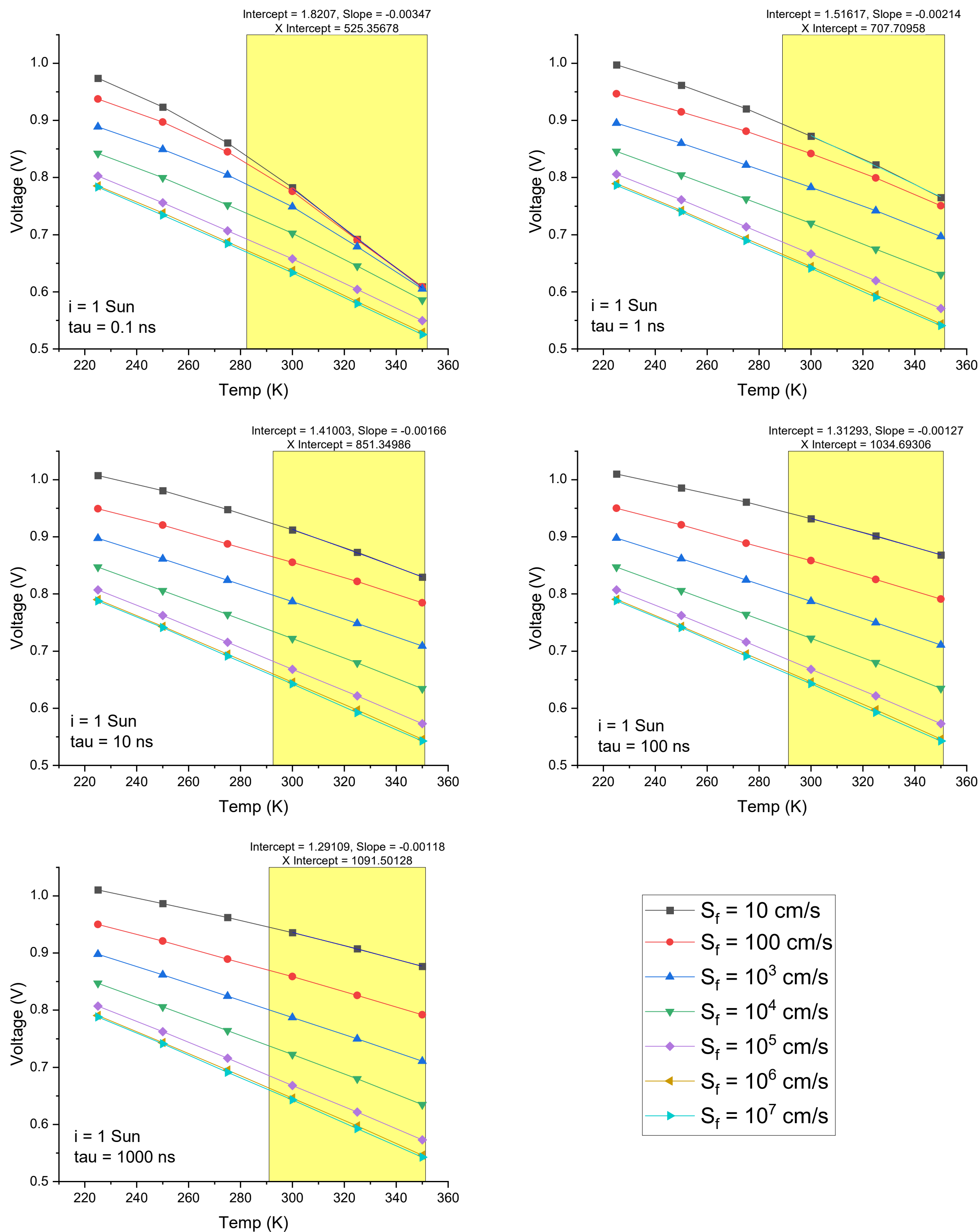

Figure 11 V_{oc} vs. T for CBO = -0.2 eV, i = 1 Sun

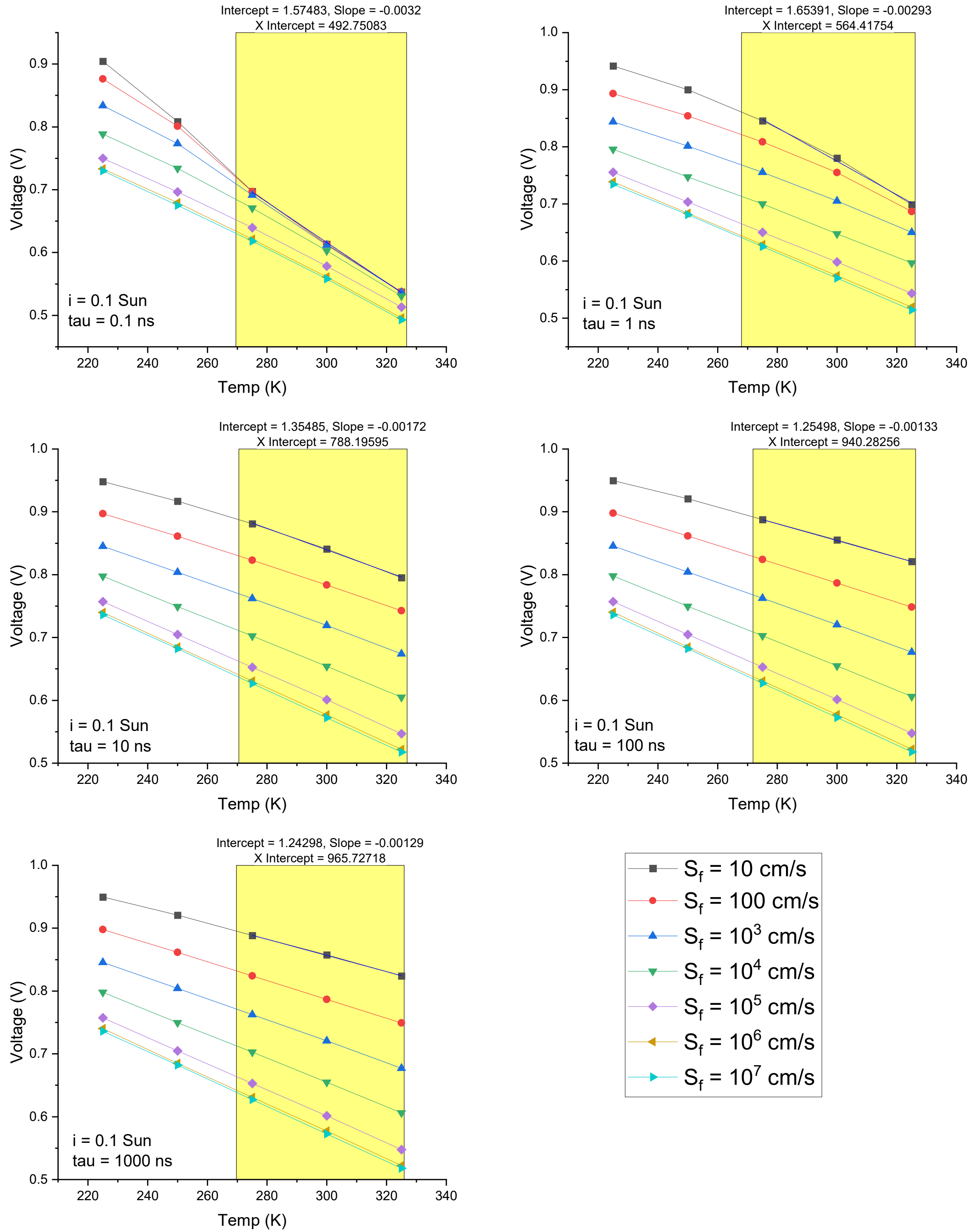

Figure 12 V_{oc} vs. T for CBO = -0.2 eV, i = 0.1 Sun

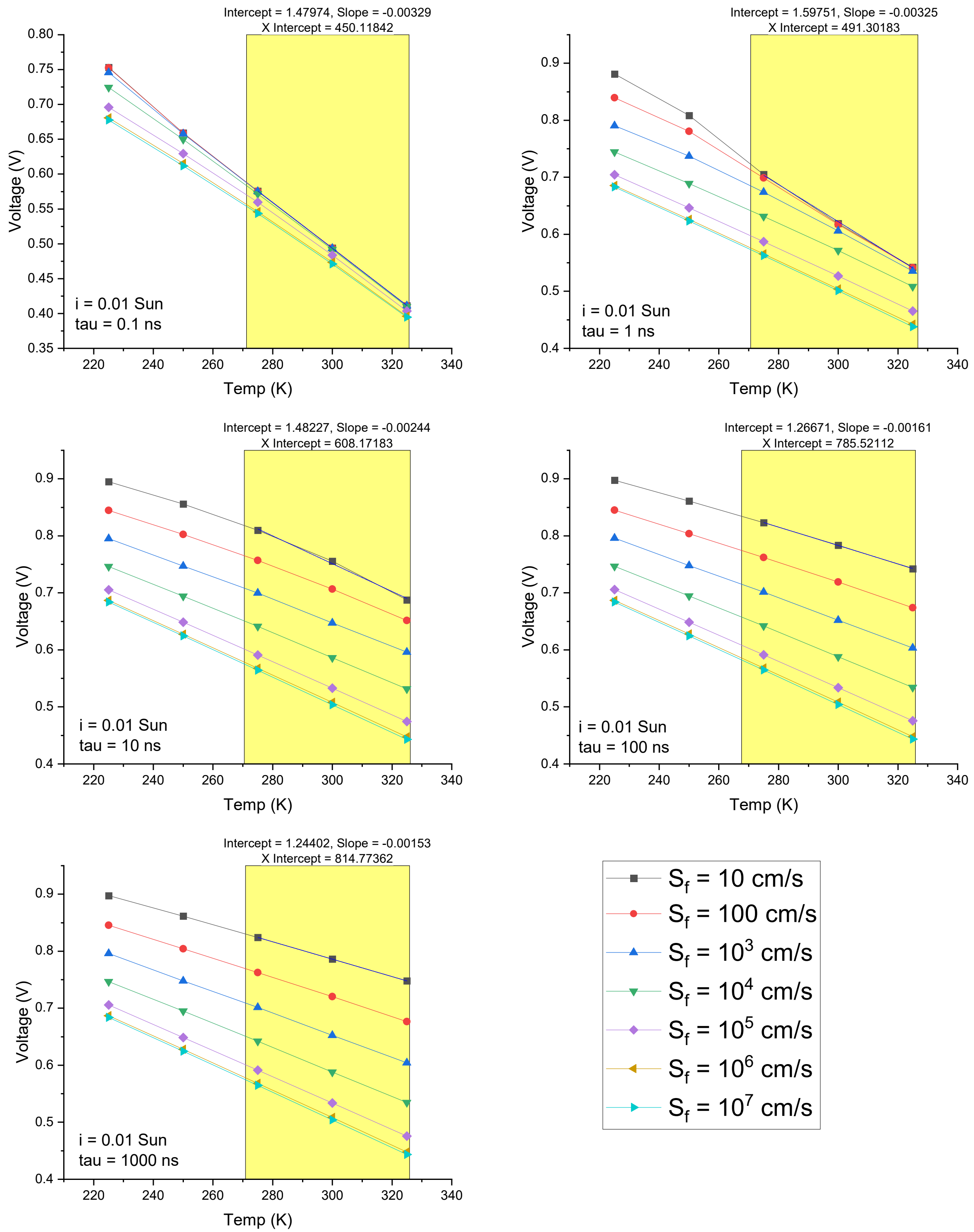

Figure 13 V_{oc} vs. T for CBO = -0.2 eV, i = 0.01 Sun

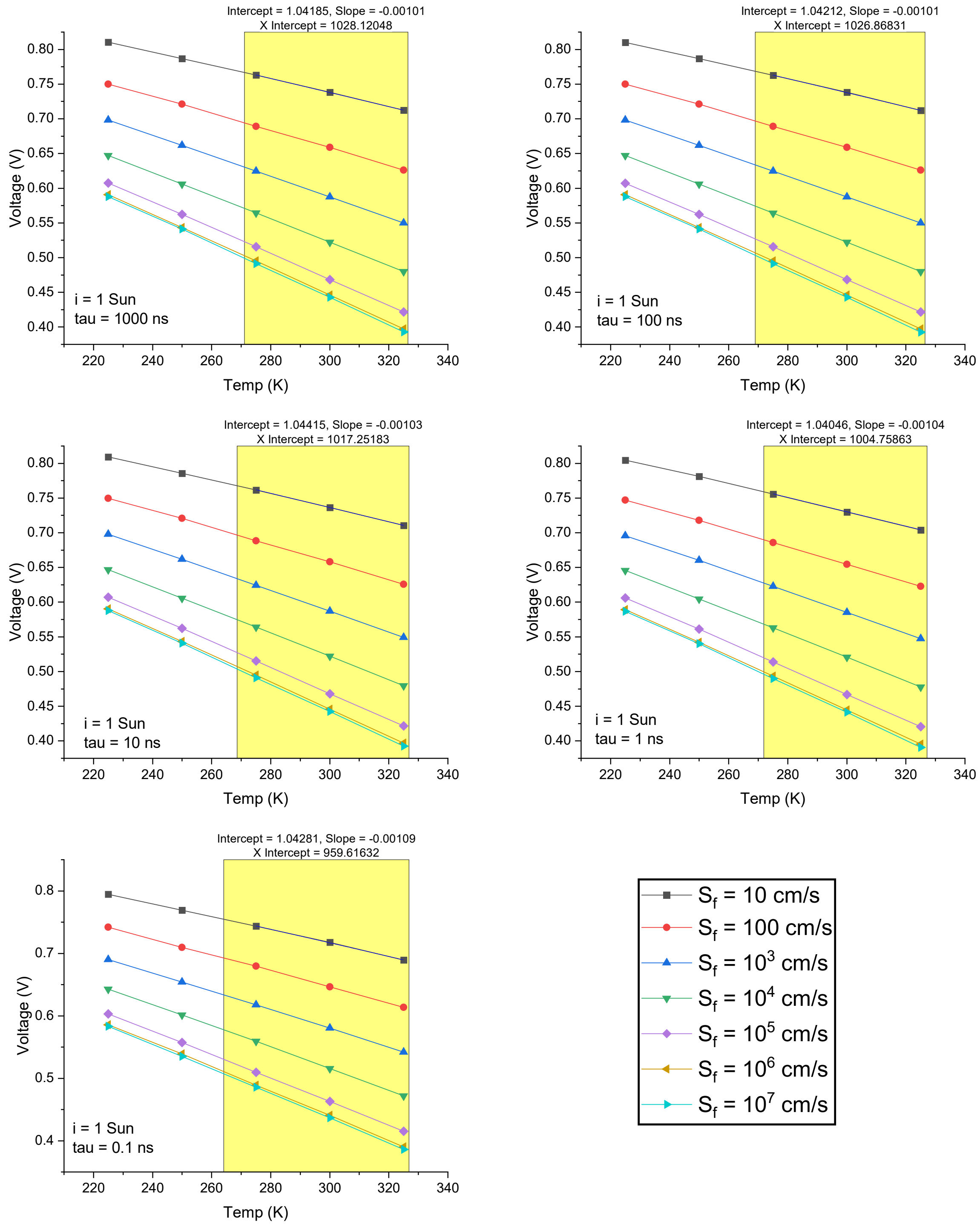

Figure 14 V_{oc} vs. T for CBO = -0.4 eV, i = 1 Sun

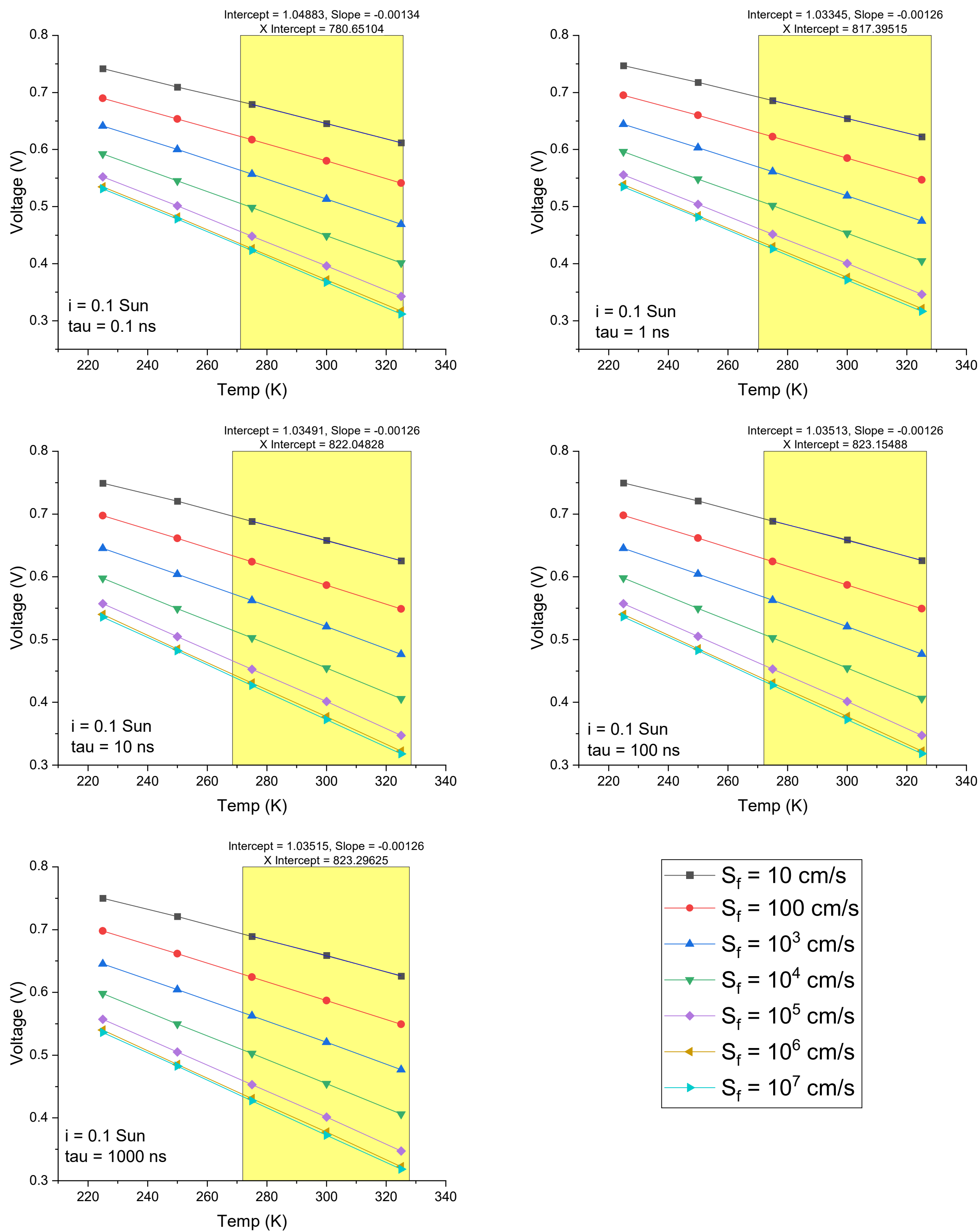

Figure 15 V_{oc} vs. T for CBO = -0.4 eV, i = 0.1 Sun

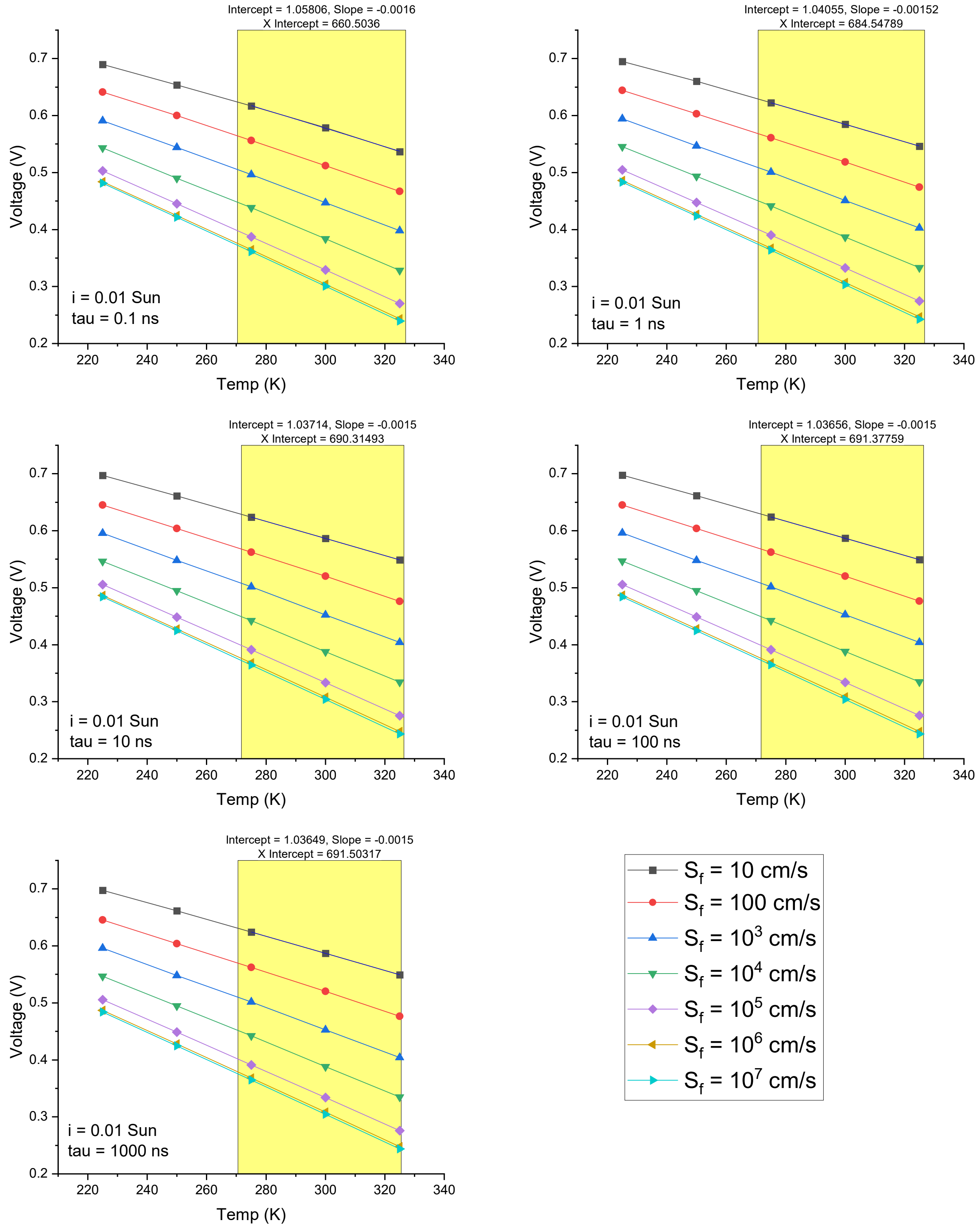

Figure 16 V_{oc} vs. T for CBO = -0.4 eV, i = 0.01 Sun